

1-1-2023

## Influence of surface cracking, anchor head profile, and anchor head size on cast-in headed anchors in geopolymer concrete

Trijon Karmokar  
*Edith Cowan University*

Alireza Moyheddin  
*Edith Cowan University*

Follow this and additional works at: <https://ro.ecu.edu.au/ecuworks2022-2026>



Part of the [Civil and Environmental Engineering Commons](#)

---

[10.1007/s11709-023-0987-5](https://doi.org/10.1007/s11709-023-0987-5)

Karmokar, T., & Moyheddin, A. (2023). Influence of surface cracking, anchor head profile, and anchor head size on cast-in headed anchors in geopolymer concrete. *Frontiers of Structural and Civil Engineering*, 17(8), 1163-1187.

<https://doi.org/10.1007/s11709-023-0987-5>

This Journal Article is posted at Research Online.

<https://ro.ecu.edu.au/ecuworks2022-2026/3253>

# Influence of surface cracking, anchor head profile, and anchor head size on cast-in headed anchors in geopolymer concrete

Trijon KARMOKAR\*, Alireza MOYHEDDIN

School of Engineering, Edith Cowan University, Perth 6027, Australia

\*Corresponding author. E-mail: tkarmoka@our.ecu.edu.au

© The Author(s) 2023. This article is published with open access at link.springer.com and journal.hep.com.cn

**ABSTRACT** In this study, the concrete cone capacity, concrete cone angle, and load–displacement response of cast-in headed anchors in geopolymer concrete are explored using numerical analyses. The concrete damaged plasticity (CDP) model in ABAQUS is used to simulate the behavior of concrete substrates. The tensile behavior of anchors in geopolymer concrete is compared with that in normal concrete as well as that predicted by the linear fracture mechanics (LFM) and concrete capacity design (CCD) models. The results show that the capacity of the anchors in geopolymer concrete is 30%–40% lower than that in normal concrete. The results also indicate that the CCD model overestimates the capacity of the anchors in geopolymer concrete, whereas the LFM model provides a much more conservative prediction. The extent of the difference between the predictions by the numerical analysis and those of the above prediction models depends on the effective embedment depth of the anchor and the anchor head size. The influence of concrete surface cracking on the capacity of the anchor is shown to depend on the location of the crack and the effective embedment depth. The influence of the anchor head profile on the tensile capacity of the anchors is found to be insignificant.

**KEYWORDS** cast-in anchor, concrete cone capacity, geopolymer concrete, head size, surface crack, anchor profile

## 1 Introduction

### 1.1 Cast-in headed anchors

Cast-in headed anchors subjected to tensile loading may experience steel- or concrete-related failures. The anchor strength under steel failure is directly proportional to the yield stress (or in the case of high-strength steel, the ultimate strength) of the steel and the cross-sectional area of the anchor shaft. Concrete-related failures, such as concrete cone and concrete splitting failures, exhibit more complex behaviors than steel failure. Of all the failure modes, concrete cone failure is the most common failure mode of cast-in anchors and generally occurs when the tensile capacity of the concrete is exceeded [1]. The first design model of cast-in anchors failing under a concrete cone was adopted by ACI Committee 349 in the mid-1970s [2]. In 1989, a study [3] using linear fracture

mechanics (LFM) revealed that the concrete cone capacity ( $N_{u,LFM}$ ) of anchors depended on the elastic modulus ( $E_c$ ) and the Mode 1 fracture energy of the concrete substrate,  $G_F$  (Eq. (1)). Measuring the Mode 1 fracture energy of concrete is intricate and requires highly sophisticated equipment. In 1995, Fuchs et al. [4] proposed the concrete capacity design (CCD) model. The CCD model uses the most commonly measured concrete properties, the average uniaxial compressive strength of concrete (cylinder) at the age of testing ( $f_{cm}$ ) and effective embedment depth of the anchors ( $h_{ef}$ ), to predict the concrete cone capacity ( $N_{u,CCD}$ ) (Eq. (2)). In Eq. (2),  $f_{cm}^{0.5}$  is used to approximate the tensile strength of concrete [1]. The CCD model is still widely used in most design standards [5–8] and as a benchmark by researchers.

$$N_{u,LFM} = 2.1 \cdot h_{ef}^{1.5} \sqrt{E_c \cdot G_F} \cdot N, \quad (1)$$

$$N_{u,CCD} = 16.8 \cdot \sqrt{f_{cm}} \cdot h_{ef}^{1.5} \cdot N. \quad (2)$$

The factors that influence the behavior of both cast-in and post-installed anchors include the type of concrete substrate [9–20], presence of cracks in the substrate concrete [21–24], reinforcement in the concrete [22,25–27], age of the concrete [28–34], varying thickness of the substrate [27,35], and presence of void formers in the substrate [32,36]. One geometric parameter that specifically influences the capacity of cast-in headed anchors is the head size ratio [27,35,37–40]. Further research on the specific parameters affecting the behavior of post-installed and cast-in anchors can be found in Refs. [41–50].

Studies conducted on cracked concrete [27,51,52] consider that cracks propagate through the entire depth of the slab, and the tensile stresses are only transferred through the orthogonal surface reinforcement. Correspondingly, standard prediction models [5–8] have used these studies to adjust their equations to incorporate the reduction in anchor capacity due to cracked concrete, which is applied through a reduction of ~30% in the constants used in Eqs. (1) and (2). To the best of our knowledge, there is no literature on the effects of concrete surface cracking on the tensile behavior of anchors.

In addition to the effective embedment depth and the concrete material properties, such as  $f_c$ ,  $E_c$ , or  $G_F$  (some of these are taken into consideration by different prediction models), the tensile capacity of headed anchors and the diameter of the concrete cone in the concrete cone failure mode have also been shown to depend on the ratio of the bearing stress over the anchor head ( $\sigma_b$ ) to the uniaxial compressive strength of concrete ( $f_c$ ) [35,37,38]. This is referred to as the anchor head size ratio ( $\sigma_b/f_c$ ) in the current study. The bearing stress ( $\sigma_b$ ) used in this ratio is calculated by dividing the anchor capacity, determined by Eq. (2), by the bearing area of the anchor ( $A_b$ ). According to Nilforoush et al. [35], the anchor head size can be categorized as small, medium, and large when  $\sigma_b/f_c \approx 20$ , 11, and 4, respectively. Note that in this study, the term anchor head diameter is not the same as the anchor head size.

Studies conducted on anchors with varying anchor head size ratios at similar effective embedment depths showed a significant influence on the concrete cone capacity of the anchor, which was not captured by any of the prediction equations [35,38]. The numerical study conducted by Ozbolt et al. [38] demonstrated that the CCD model underestimated the capacity of large-headed anchors by up to 111%. Similarly, Nilforoush et al. [35] stated that the CCD model underestimated the capacity of large-headed anchors by up to 15%, whereas small-headed anchors were predicted accurately by the CCD model. Therefore, they suggested applying a modification factor ( $\Psi_{AH}^{0.1}$ ) to Eq. (2) to incorporate the influence of the anchor head size ratio. Because Eqs. (1) and (2) assume that the bearing stress on the anchor head is  $15f_{cm}$ , the

modification factor is applicable to both equations.

$$N_{u,AH} = \Psi_{AH}^{0.1} \cdot N_{u,CCD} \text{ or } N_{u,LFM} \cdot N, \quad (3)$$

where  $\Psi_{AH} = \frac{A_b}{A_b^0}$ ;  $A_b^0 = \frac{N_{u,CCD} \text{ or } N_{u,LFM}}{15f_{cm}}$ , mm<sup>2</sup>;  $A_b^0$  is the bearing area over the anchor head such that the bearing stress is 15 times the uniaxial compressive strength of concrete and  $\Psi_{AH}$  is the modification factor for the anchor head size

## 1.2 Geopolymer concrete

Geopolymer concrete has attracted interest in the construction industry as an eco-friendly alternative to normal concrete. However, one of the main issues with geopolymer concrete is the health and safety concerns that arise from the hazardous materials in such concrete mixes, such as fly ash, blast furnace slag, and highly concentrated alkaline hydroxides and silicates. Moreover, geopolymer concrete is more prone to drying shrinkage than normal concrete [53,54]. Therefore, geopolymer concrete is considered more suitable for the precast industry, where curing occurs under more controlled environments. It should be noted that the term “geopolymer concrete” in the current study refers exclusively to fly ash-based geopolymer concrete. In this type of geopolymer concrete, workability is usually an issue, and the addition of water to improve workability lowers the mechanical properties of the concrete [55,56]. The workability of geopolymer concretes depends on the binding material, aggregate size, and alkaline solution used [57]. Many studies [58–61] have shown that the addition of blast furnace slag to fly ash provides significantly better mechanical properties; however, it further reduces the workability of the concrete. According to the results obtained by Yousefi Oderji et al. [61], substituting 15% of the fly ash with blast furnace slag yielded the best mechanical properties with a tolerable loss of workability. Bouaissi et al. [57] reported that binding materials including a mix of fly ash, blast furnace slag, and high-magnesium nickel slag improved the workability of concrete by providing a dense microstructure, resulting in a significant increase in the compressive strength compared to fly ash-based geopolymer concrete. A recent study conducted by Ren et al. [62] found that the use of natural seawater in geopolymer concrete prolonged the setting time and hence provided a slight improvement in workability; it further reduced the amount of heat released during the geopolymerization process. In terms of mechanical properties, the use of seawater in geopolymer concrete results in better compressive strength but lower flexural strength compared to those of geopolymer concrete mixes with deionized water.

Several studies have been conducted to identify the most effective type of superplasticizer to improve the

workability and mechanical properties of geopolymer concrete binding materials, such as fly ash [63,64], slag [65], and a combination of both [60]. A recent comprehensive literature review by Nguyen et al. [66] concluded that with the exception of naphthalene base, most types of superplasticizers produce a chemically unstable state of matter when induced into a highly alkaline environment (i.e., when employed with alkaline activators) and do not provide any improvement in either the mechanical properties or workability of geopolymer concrete.

The type of alkaline activator, percentage of composite alkaline solutions, and alkaline solution-to-binder ratio significantly influence the mechanical characteristics, workability, and microstructure of geopolymer concrete [56]. Increasing the sodium hydroxide (NaOH) concentration from 8 to 16 mol/L results in an approximately twofold increase in the compressive strength [67–69]; similarly, increasing the alkaline solution-to-binder ratio from 0.3 to 0.5 increases the compressive, flexural, and tensile strengths of geopolymer concrete, and also improves the workability [70–72]. Furthermore, adding sodium silicate ( $\text{Na}_2\text{SiO}_3$ ) to the commonly used sodium hydroxide (NaOH) improves the mechanical properties of geopolymer concrete compared to using only NaOH. Additionally, increasing the sodium silicate content increases the silicates-to-aluminum and sodium-to-aluminum ratios, leading to greater production of sodium aluminosilicate gel, which indicates a denser geopolymer microstructure [73–75].

Finally, studies have shown that the mechanical properties of geopolymer concrete are highly susceptible to the curing temperature [56,76–78]. When cured at elevated temperatures, geopolymer concrete shows a significant increase in compressive strength compared to curing under ambient temperature. Muhammad et al. [76] reported that the ideal temperature to obtain the highest compressive strength is 80 °C, while the compressive strength decreases with any further increase in curing temperature beyond 80 °C [79]. According to studies conducted on geopolymer concrete cured at ambient temperature [58,80], the elastic modulus and fracture energy of geopolymer concrete are significantly lower than those of normal concrete with a similar compressive strength. Therefore, given that the tensile capacity of anchors depends on the elastic modulus and fracture energy [3], it is reasonable to postulate that there may be a reduction in the capacity of anchors installed in geopolymer concrete compared to those installed in normal concrete. Recent studies [81–83] have shown that the inclusion of fibers and microsilica in geopolymer concrete improves the fracture energy at the cost of workability.

In this study, the mechanical properties of fly ash-based geopolymer concrete cured under ambient temperature

and without any fibrous material were used to investigate the tensile behavior of cast-in anchors, with an emphasis on the influences of substrate surface cracking due to shrinkage of the geopolymer concrete, the anchor head profile, and the anchor head size on the tensile behavior of the anchors. Five series of numerical analyses (more than 40 analyses in total) were performed and compared in this study in addition to the analyses initially conducted for calibration purposes.

This study is motivated by the gap in the available literature regarding the tensile performance of anchors in geopolymer concrete. Geopolymer concrete employs other cementitious materials such as fly ash or blast furnace slag as complete replacements for cement in the concrete mix. Therefore, with the growing awareness of global warming and increasing interest in protecting the environment, the demand for geopolymer concrete has increased significantly. Recently, precast geopolymer concrete planks were used in two major projects in Australia: Brisbane West Wellcamp Airport and the University of Queensland's Global Change Institute building [84]. Given that cast-in headed anchors are the most commonly used type of anchor for lifting precast concrete elements, the current study aims to provide insight into the tensile performance of such anchors in geopolymer concrete.

---

## 2 Material constitutive models and modeling technique

The ABAQUS implicit procedure is used for the numerical/finite element analysis of the anchors in this study. Two-dimensional (2D) axisymmetric models are created, which are more efficient than three-dimensional (3D) models in terms of computational run times. In this study, only the concrete cone failure mode is considered. An anchor failing through concrete cone failure, when not affected by the edge effect or the thickness of the substrate, is theoretically an axisymmetric/rotationally symmetric problem. However, during experiments, the cone always forms an asymmetric shape because the concrete is not completely homogenous or contains imperfections related to installation. Such irregularities lead to either larger or smaller cones with cone angles that are smaller or larger, respectively, than the theoretical values. This also means that there is a variation in the cone angle around the same cone. Consequently, the actual measured capacity may be greater or less than the values predicted by the models (such as the CCD model), which assume an ideal symmetric cone shape.

In theory, assuming that a 3D model and its counterpart 2D model use material constituent models with the same level of detail, perfection, and nonlinearity (also

assuming that such material models are isotropic and homogenous), which is the case here, and that there is symmetry in the applied load, boundary conditions, and geometric layout, one would expect similar results from (properly constructed) 2D and 3D models. The 2D axisymmetric models are calibrated against three experimental studies from the literature and compared with the experimental results obtained in this study to verify their accuracy (Section 3 and Subsection 5.1). It should be noted that because all of the anchors from these studies failed owing to cone failure, properly established 2D models can be as efficient as 3D models, and this would also apply to the steel and pull-out failure modes of an anchor. However, 2D models will be inferior to 3D models if the failure mode of the anchor is splitting failure, owing to the reduced concrete substrate thickness. The limitations of 2D models are discussed further in Subsection 4.1.

### 2.1 Steel material

The steel used to manufacture the cast-in headed anchors is assigned a bilinear elastic-plastic model. The yield stress and ultimate strength are 550 and 650 MPa, respectively. The modulus of elasticity and Poisson's ratio are 210 GPa and 0.3, respectively.

### 2.2 Concrete material

ABAQUS offers three unique material constitutive models for concrete: concrete damaged plasticity (CDP), concrete smeared cracking, and concrete brittle cracking. Among the three material models suitable for concrete material modeling in ABAQUS, the CDP material model is the most widely utilized because of its high reliability [85], improved calculation efficiency, and good agreement with experimental results [64,65]. The other two material models, concrete smeared cracking and concrete brittle cracking, are not only more complex to use, but also make the convergence of numerical solutions more challenging, with the latter defeating the purpose [86,87]. CDP is based on isotropic damaged elasticity and isotropic tensile and compressive plasticity [88]. Given that the same model can be used in both 2D and 3D, one would not expect any compromise in the accuracy of the results from a material modeling perspective. Therefore, a 2D axisymmetric model can be used to represent a 3D model, as discussed in Section 2. In this model, the nonlinear response of concrete is represented using the plasticity and damage theory, whereby the plasticity model represents the realistic deformation of concrete, and the damage model represents the reduction in elastic stiffness of the concrete [89]. It is essential to include both the plasticity and damage models to simulate realistic nonlinear responses of concrete [90].

The compressive stress beyond the initial elastic range is defined as a function of the inelastic (crushing) strain, where the inelastic strain (related to any given stress) is the difference between the total strain and the maximum elastic strain within the elastic range (undamaged material). For the tensile behavior, the fracture energy cracking criterion is considered the most suitable approach to avoid unreasonable mesh sensitivity. The compressive and tensile damage models are developed using the methodology proposed by Alfarah et al. [89].

Normal concrete is modeled using relevant constitutive prediction models [5,89,91–93]. Relevant material tests were conducted on geopolymer concrete to determine the required material properties, namely  $f_{cm}$ , the stress–strain curve,  $E_c$ , concrete average uniaxial tensile strength ( $f_{tm}$ ), and  $G_F$ , for the numerical analyses. The relevant experimental setup and test procedures are described in [94]. Figure 1 shows the compressive ( $\sigma_c$ ) and tensile stress ( $\sigma_t$ )–strain curves for normal and geopolymer concretes, along with the relevant compressive ( $d_c$ ) and tensile damage ( $d_t$ ) curves used in the current numerical models. Table 1 lists the mechanical properties of the normal and geopolymer concretes used in the numerical analyses in this study.

The CDP constitutive model also requires some plasticity parameters to be input, namely the dilation angle (DA), eccentricity, Ratio of the initial equi-biaxial compressive yield stress to the initial uniaxial compressive yield stress ( $\sigma_{b0}/\sigma_{c0}$ ), Ratio of the second stress invariant on the tensile meridian ( $K_c$ ), and the viscosity parameter (VP). The DA and VP are fine-tuned during the calibration process to balance the accuracy and convergence of the numerical analyses because they are highly sensitive to the models (Subsections 3.1 and 3.2). All of the other parameters are defined according to the recommendations of the ABAQUS documentation [88]. After calibration, all such parameters are kept unchanged in all subsequent analyses for both the normal and geopolymer concretes. Table 2 lists the values used for the plasticity parameters in this study.

### 2.3 Contact surfaces and boundary conditions

The surface-to-surface contact between the anchor and concrete is defined using the normal interactions available in ABAQUS. The normal interaction contact property is based on the Lagrange multiplier method and allows separation between two surfaces in contact owing to their relative displacements. Because the load-transfer mechanism for cast-in headed anchors is mainly due to mechanical interlocking [1], the load transfer due to friction is ignored in the models presented here; hence, the two surfaces are considered frictionless. The nodes are adjusted to remove any initial penetration, and a finite-sliding contact formulation is used to establish the

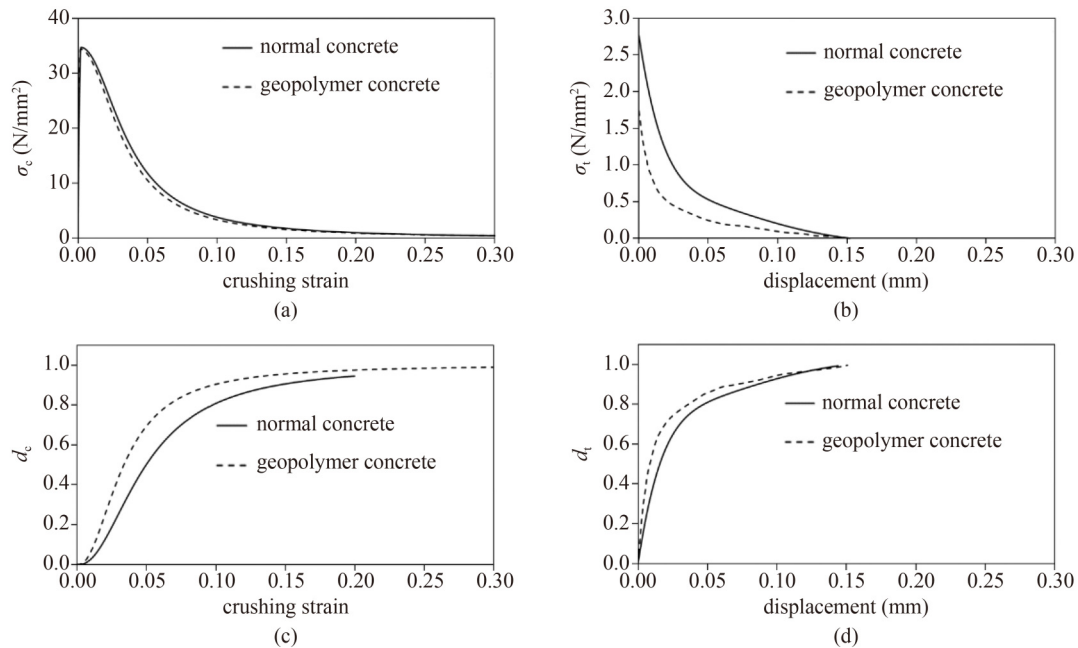


**Fig. 1** Material constitutive models for normal and geopolymer concrete with  $f_{cm} = 34$  MPa: (a) compressive stress vs. crushing strain; (b) tensile stress vs. displacement; (c) compressive damage variable vs. crushing strain; (d) tensile damage variable vs. displacement.

**Table 1** Material properties used in numerical analyses

material property	normal concrete	geopolymer concrete
$f_{cm}$ (MPa)	34	34
$f_{tm}$ (MPa)	2.7	2.6
$E_c$ (MPa)	26608	22987
$G_F$ (N/m)	82.4	41.4

**Table 2** Concrete plasticity parameters used for all numerical analyses

plasticity parameter	value	references
DA	35°	Subsection 3.1
eccentricity	0.1	[88]
$\sigma_{b0}/\sigma_{c0}$	1.16	[88]
$K_c$	0.67	[88]
VP	0.000025	Subsection 3.2

relationship between the primary and secondary surfaces. In all cases, displacement-controlled loading is adopted, and incremental vertical displacements are applied to the top surface of the anchor head. The vertical boundary condition represents the base of a circular loading frame. The distance between the anchor and the boundary condition for all numerical analyses is 270 mm from the center of the anchor (Fig. 2).

2.4 Concrete damaged plasticity model: mesh dependency

One of the most common techniques used to obtain mesh-independent results is the crack band approach by Bažant and Oh [95]. For concrete modeling, the crack band

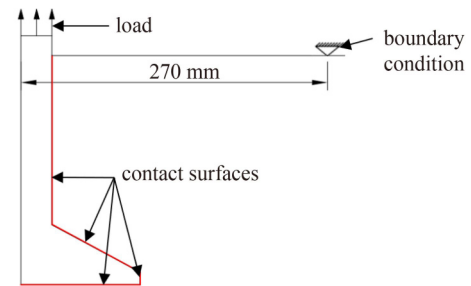


**Fig. 2** Contact surfaces, boundary condition, and load locations (not to scale).

approach is partly inspired by Hillerborg et al. [96] fracture energy cracking criterion. According to Hillerborg et al. [96], the stresses near the crack opening do not fall to zero immediately after cracking but decrease with increasing crack width ( $w$ ). According to this approach, the behavior of concrete can be characterized based on the stress–displacement curve, which yields mesh-independent load–displacement results [88,96,97]. In the CDP model, the fracture energy cracking model is used only for the tensile behavior of concrete and is defined using post-failure stress-to-crack displacement data. The mesh sensitivity is demonstrated in Subsection 2.5.

2.5 Mesh sensitivity

The use of 2D axisymmetric models significantly reduces computational runtimes. Therefore, compared to a 3D model, a finer mesh can be used to add more precision to the conducted analyses while maintaining substantially

shorter runtimes. Mesh sensitivity is evaluated in conjunction with the calibration process, as presented in Section 3. Figure 3 shows the meshes in three models used to explore the mesh sensitivity. The mesh size near the expected fracture zone is the finest at 1, 3, and 5 mm in models (a)–(c), respectively, and gradually increases to 20 mm near the free edges. The anchor mesh size also varies as 2, 4, and 6 mm in models (a)–(c), respectively, to improve the interaction between the anchor and concrete substrate. The load–displacement curves show that while all of the models produce the same ultimate load, only the strain softening observed in models (a) and (b) is similar. While the results obtained from models (a) and (b) are identical, model (a) took approximately four times longer to complete. Therefore, it was decided that the mesh used in model (b) had the optimum size.

### 3 Calibration of the numerical models

The numerical models were calibrated by comparing their results with those of the experiments. For this purpose,

three independent experimental studies on headed anchors installed in normal concrete were selected from the literature. The experiments were carefully selected such that they provided a wide range of effective embedment depths, anchor head size ratios, and mechanical properties of concrete (Table 3). Load–displacement curves and crack patterns were considered for the comparison and calibration.

The main objective of the calibration process was to determine the optimum DA and VP for use throughout the numerical study because the first trial of the numerical simulations showed a high level of sensitivity of the results to these two plasticity parameters.

#### 3.1 Dilation angle

Dilation refers to the ratio of the rate of volume increase to the rate of shear deformation when a material is in the plastic state. In the CDP model, dilation is specified using the plasticity parameter of the DA. This is one of the most important parameters that must be specified in the CDP model to obtain accurate results. Some previous studies

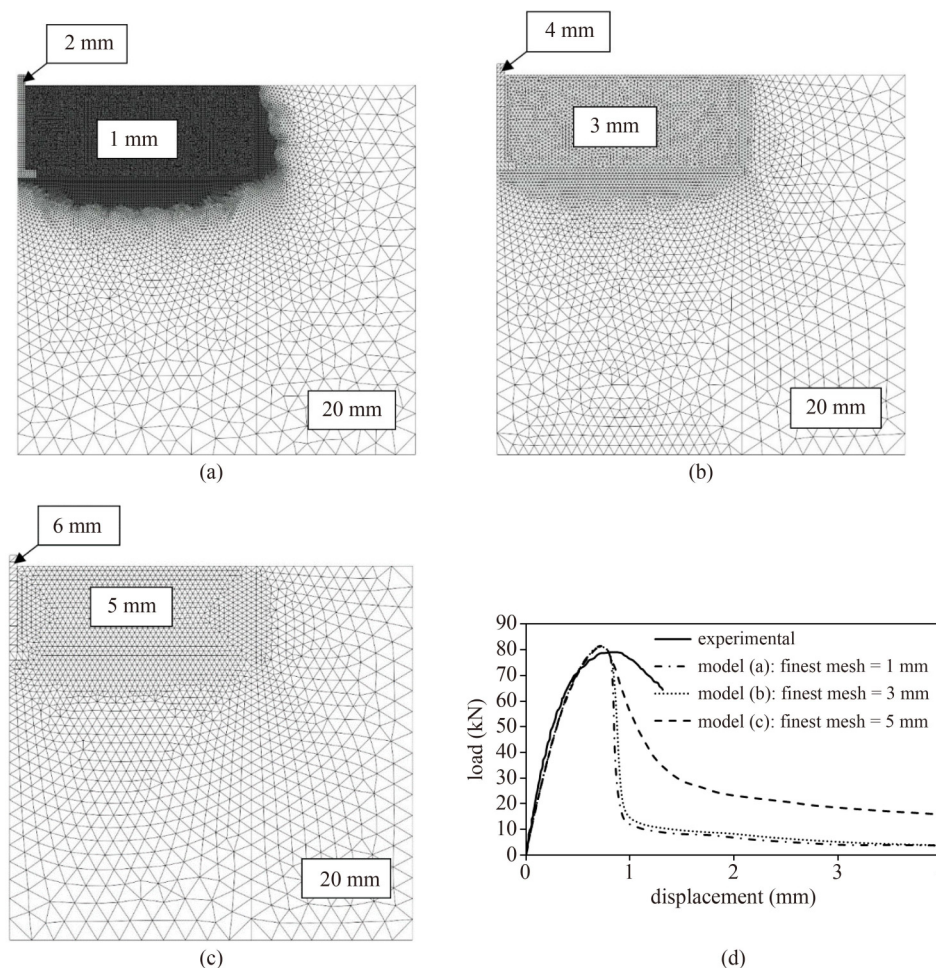


**Fig. 3** Mesh sensitivity analyses and corresponding load–displacement curves: (a) finest mesh used: 1 mm; (b) finest mesh used: 3 mm; (c) finest mesh used: 5 mm; (d) load–displacement curves for different mesh sizes.

**Table 3** Main parameters of the experiments used to calibrate the numerical models

model ID	$\sigma_b/f_c$	$h_{ef}$ (mm)	$f_{cm}$ (MPa)	Ref.
calibration 1	2.9	50	32	[9]
calibration 2	2.3	80	42	[29]
calibration 3	8.4	220	34	[11]

used different DA values ranging from 5° to 45°, with the majority recommending a DA between 30° and 40° [98–102]. According to Malm [102], lower DAs result in brittle behavior of the concrete, whereas higher angles result in an increase in ductility. A recent study conducted by Wosatko et al. [103] stated that for higher DAs (> 35°), cracks tended to spread, deviating from the experimental observations, even when the experimental and theoretical load–displacement graphs were in good agreement. Therefore, Wosatko et al. [103] suggested that to demonstrate that the numerical model is in agreement with the experimental results, not only the load–displacement curves but also the crack patterns should be compared.

Three different DAs (25°, 30°, and 35°) are used in the three calibration models in the current study. Figure 4 shows the load–displacement curves and crack patterns of the anchors subjected to tensile loading along with their corresponding experimental results. The contour crack lines show the numerical results, whereas the solid crack line indicates the experimentally observed crack/concrete cone. These results demonstrate that the DA plays a significant role not only in capturing the correct crack patterns and cone size but also in the ultimate capacity of the anchor and the displacement at which the ultimate capacity is reached. A DA of 25° provides the lowest ultimate capacity of the anchor and a steeper concrete cone crack compared with the results obtained for DAs of 30° and 35°. This is similar to the observations made by Malm [102]. In this study, a DA of 35° provides the most accurate ultimate capacity and concrete cone crack pattern, with a maximum error of 12% for the ultimate capacity. Therefore, a DA of 35° is used for all of the numerical analyses.

### 3.2 Viscosity parameter

The viscoplastic regularization technique is typically used to solve convergence issues related to the stiffness degradation of materials that exhibit softening behavior. This is achieved by triggering the algorithmically consistent tangent stiffness matrices to become positive for small time increments, which would otherwise be negative and result in negative eigenvalues in the system and convergence errors. ABAQUS uses an iterative process to identify the minimum time increment required to obtain a stable solution.

In the CDP material model, viscoplastic regularization

is controlled using the VP. According to the Abaqus documentation [88], to obtain convergence without compromising the accuracy of the results, the VP selected should be smaller than the characteristic time increment. Therefore, the minimum time increment required to obtain a stable solution must be determined before selecting an appropriate VP. The minimum time required to obtain a stable solution is automatically calculated by Abaqus using an iterative process.

For all of the numerical analyses in this study, the minimum time increment required to obtain a stable/converged solution is  $1 \times 10^{-4}$  s. Similar to the calibration of the DA, each of the three numerical models was tested using three different VPs, and the load–displacement curves and crack patterns were compared for each case. In Fig. 5, a VP value of 0.00025, which is slightly larger than the minimum time increment, results in a dispersed crack pattern and an approximately 30%–50% higher capacity in all three cases. In contrast, VP values of 0.000025 and 0.0000025, which are both smaller than the minimum time increment, show load–displacement curves and crack patterns comparable to those of the experiments. Accordingly, a VP of 0.000025 is selected because it is the most computationally efficient.

## 4 Assumptions in the numerical models

In this section, the numerical results are compared with the experimental results obtained in this study, as presented in Table 4. It should be noted that manufacturers of cast-in headed anchors commonly identify the anchors by their working load limits (WLLs) in tonnes (T). For example, a 1.3T anchor has a WLL (capacity) of 1.3 t. Table 4 presents the anchor shank diameter ( $d$ ), head diameter ( $d_h$ ), and head size ratio ( $\sigma_b/f_c$ ) of all the anchors used in this study. Further details of the experimental setup and program can be found in Karmokar et al. [94]. The Serie A mentioned in this study is part of the validation process, and the results are discussed in Subsection 5.1.

### 4.1 Surface crack modeling

To establish a systematic and critical approach to identify the change in the behavior of anchors due to surface cracking, a crack with a depth of 10 mm and width of 0.2 mm is introduced at varying distances from the center of the anchor ( $L_{cr}$  in Fig. 6) to investigate the effect of such cracks on the initiation/propagation of cracks during cone failure of the anchor. To model the cracks on the surface, a discontinuity (U-shaped notch) is created in the mesh (Fig. 6). The width and depth of the notches are equal to the maximum crack width and depth, respectively, were measured in the laboratory on the

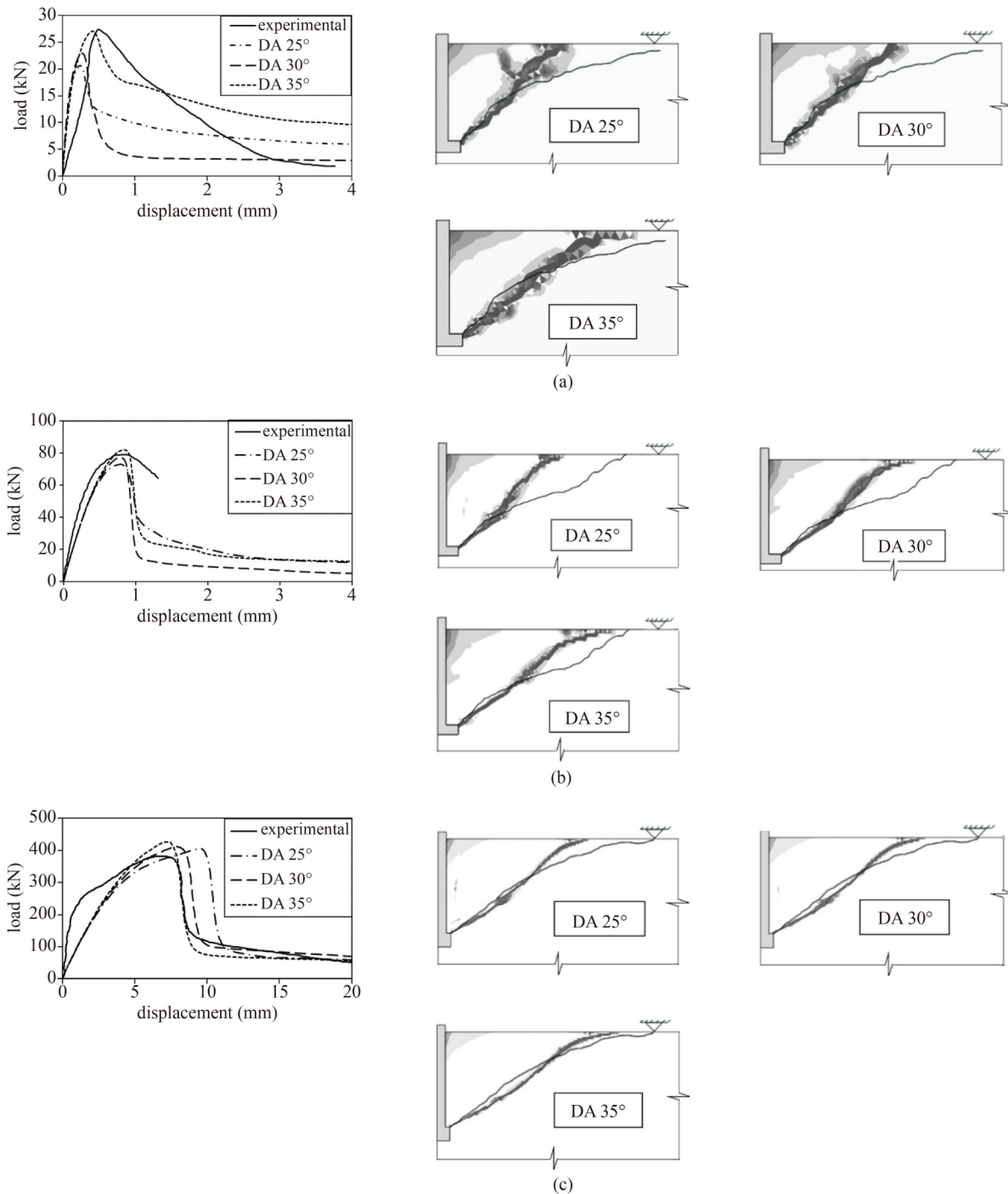


**Fig. 4** Load–displacement curves and crack patterns for models with varying DAs: (a) model ID: calibration 1; (b) model ID: calibration 2; (c) model ID: calibration 3.

surfaces of the geopolymer concrete slabs. These dimensions magnify the effect of such cracks, which are in most cases smaller in width, depth, or both. The other amplifying effect of such a crack in the constructed 2D model is the continuity of the crack, as it represents a continuous circular crack on the surface rather than staggered crack lines of limited lengths in different directions. Therefore, it is expected that the adverse effects of surface cracking in the constructed numerical

model may be accentuated unrealistically, which may be a shortcoming of the current model. This is discussed in more detail in Subsection 5.4.

#### 4.2 Anchor profile

Cast-in headed anchors normally have either an angular anchor head (P1) or a flat head (P2), as shown in Fig. 6, where  $s_1$  is the anchor shoulder length and  $\beta$  is the angle

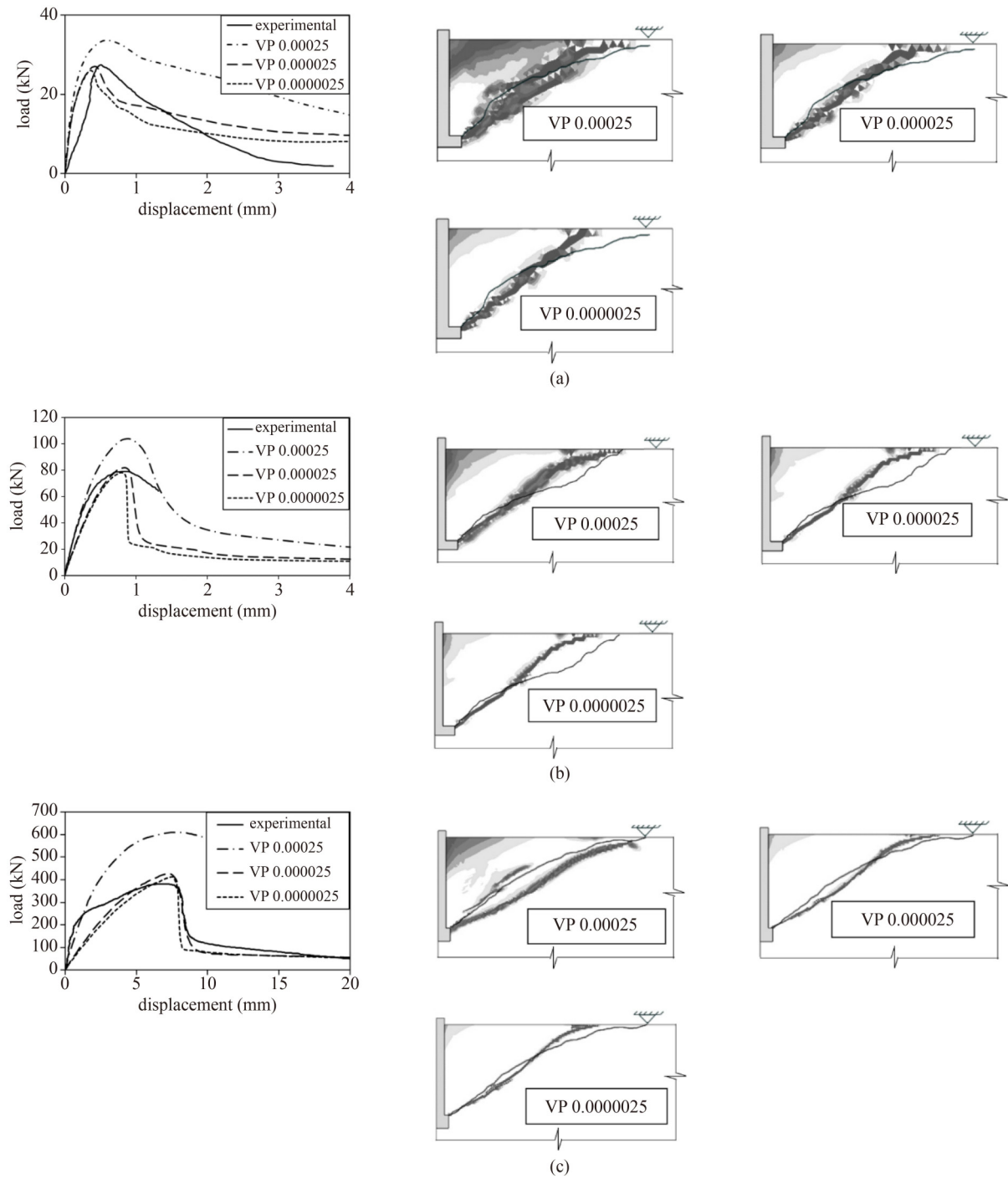


**Fig. 5** Load–displacement curves and crack patterns of models with varying VP values: (a) model ID: calibration 1; (b) model ID: calibration 2; (c) model ID: calibration 3.

**Table 4** Geometric dimensions, head size ratios, and test matrix of the experimental study

$h_{ef}$	large head											
	1.3T				2.5T				5T			
	$d$	$d_h$	$\sigma_b/f_c$	No. of tests	$d$	$d_h$	$\sigma_b/f_c$	No. of tests	$d$	$d_h$	$\sigma_b/f_c$	No. of tests
40	10	25	1.8	5	14	35	0.9	5	20	45	0.6	5
70	10	25	4.1	5	14	35	2.1	5	20	45	1.3	5
90	–	–	–	–	14	35	3.0	5	20	45	1.9	5

Note: All geometric dimensions,  $h_{ef}$ ,  $d$ , and  $d_h$ , are in mm.

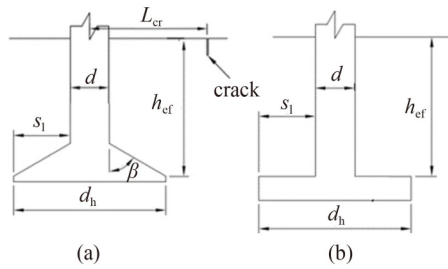


Fig. 6 Anchor head profiles: (a) P1; (b) P2.

of anchor head shoulder. Figure 7 shows the principal stress vectors in the vicinity of the anchor heads for P1 and P2 headed anchors subjected to tensile loading as an indication of the load path near the anchor head. In both cases, the principal compressive stresses on the top of the head are perpendicular to the top of the head, i.e., they tend to be in the vertical direction for P2 and in an angular direction for P1. The experimental study used anchors with an inclined head profile (P1) [94]. Therefore, for a better comparison, anchors with a similar geometric profile are used in the numerical studies, and a series of numerical analyses are conducted to investigate the effect of the anchor head profile on the performance.

### 4.3 Anchor head size

The influence of the anchor head size is investigated for both normal and geopolymer concrete. The anchor head size ratio ( $\sigma_b/f_c$ ) is kept constant at 20.0 and 9.0 for small and medium head size anchors, respectively, at all

effective embedment depths. For large-headed anchors, the anchor head size ratio varies between 0.6 and 4.1 depending on the effective embedment depth.

### 4.4 Summary of variables

A summary of the geometric dimensions and relevant head size ratios of the anchors analyzed in this study is presented in Table 5. The anchor dimensions for the small- and medium-headed anchors are inspired by the literature, and the large-headed anchors are based on the anchors used in the experimental program.

The details of the numerical models are listed in Table 6. A total of 43 simulations were conducted and divided into five series. In Serie A, the anchor sizes, effective embedment depths, anchor profiles, and geopolymer concrete properties were identical to those of the experimental test matrix. The parameters in Serie B were similar to Serie A but normal concrete of the same compressive strength was used as the substrate material, facilitating a direct comparison between the behavior of anchors in normal and geopolymer concrete. In Serie C, the effect of surface cracking on the ultimate capacity of the anchor was investigated. The difference in the behavior of the anchors as a result of the change in the anchor profile (P1 and P2) in both geopolymer and normal concrete was investigated in Serie D. Finally, Serie E was used to investigate the influence of the anchor head size on the ultimate tensile capacity and crack pattern.

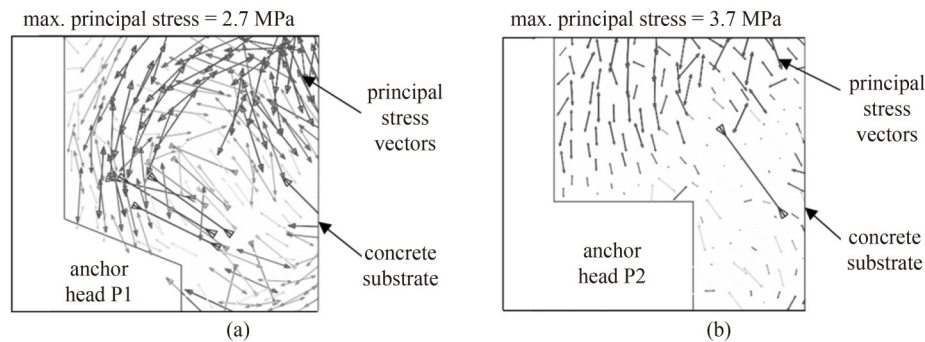


Fig. 7 Principal stress images near anchor heads subjected to tensile loading: (a) anchor head P1; (b) anchor head P2.

Table 5 Geometric dimensions and corresponding head size ratios used in the current numerical study

$h_{ef}$	small head			medium head			large head								
	$d$	$d_h$	$\sigma_b/f_c$	$d$	$d_h$	$\sigma_b/f_c$	1.3T			2.5T			5T		
							$d$	$d_h$	$\sigma_b/f_c$	$d$	$d_h$	$\sigma_b/f_c$	$d$	$d_h$	$\sigma_b/f_c$
40	10	12.0	$\approx 20$	10	14	$\approx 9$	10	25	1.8	14	35	0.9	20	45	0.6
70	14	17.5	$\approx 20$	14	21	$\approx 9$	10	25	4.1	14	35	2.1	20	45	1.3
90	20	24.5	$\approx 20$	20	29	$\approx 9$	–	–	–	14	35	3.0	20	45	1.9

Notes: All geometric dimensions,  $h_{ef}$ ,  $d$ , and  $d_h$ , are in mm, and the 1.3T, 2.5T, and 5T anchors under the large-head category are the anchor WLL in provided by the manufacturer.

**Table 6** Numerical analyses: series and models

Serie	model	anchor WLLs	anchor head size	concrete type*	$h_{ef}$ (mm)	anchor profile	$L_{cr}$ (mm)
A	1	1.3T	large	G	40	P1	–
	2	2.5T		G	40	P1	–
	3	5T		G	40	P1	–
	4	1.3T		G	70	P1	–
	5	2.5T		G	70	P1	–
	6	5T		G	70	P1	–
	7	2.5T		G	90	P1	–
	8	5T		G	90	P1	–
B	9	1.3T	large	N	40	P1	–
	10	2.5T		N	40	P1	–
	11	5T		N	40	P1	–
	12	1.3T		N	70	P1	–
	13	2.5T		N	70	P1	–
	14	5T		N	70	P1	–
	15	2.5T		N	90	P1	–
	16	5T		N	90	P1	–
C	17	2.5T	large	G	40	P1	$0.5h_{ef}$
	18	2.5T		G	40	P1	$1.0h_{ef}$
	19	2.5T		G	40	P1	$1.5h_{ef}$
	20	2.5T		G	70	P1	$0.5h_{ef}$
	21	2.5T		G	70	P1	$1.0h_{ef}$
	22	2.5T		G	70	P1	$1.5h_{ef}$
	23	2.5T		G	90	P1	$0.5h_{ef}$
	24	2.5T		G	90	P1	$1.0h_{ef}$
	25	2.5T		G	90	P1	$1.5h_{ef}$
D	26	2.5T	large	G	40	P2	–
	27	2.5T		G	70	P2	–
	28	2.5T		G	90	P2	–
	29	2.5T		N	40	P2	–
	30	2.5T		N	70	P2	–
	31	2.5T		N	90	P2	–
E	32	–	small	G	40	P2	–
	33	–	medium	G	40	P2	–
	34	–	small	N	40	P2	–
	35	–	medium	N	40	P2	–
	36	–	small	G	70	P2	–
	37	–	medium	G	70	P2	–
	38	–	small	N	70	P2	–
	39	–	medium	N	70	P2	–
	40	–	small	G	90	P2	–
	41	–	medium	G	90	P2	–
	42	–	small	N	90	P2	–
	43	–	medium	N	90	P2	–

\*Notes: G: geopolymer concrete; N: normal concrete.

## 5 Results and discussion

### 5.1 Validation of the numerical results with experimental results (Serie A)

Table 7 lists the numerical results obtained from the Serie A analyses, experimental results obtained in this study, and corresponding ratios of the numerical/experimental capacities.

As indicated in Table 7, the numerical ( $N_{u,num}$ ) and experimental ( $N_{u,exp}$ ) results exhibit a good correlation in terms of the ultimate capacities, with only two cases in which the ratio of  $N_{u,num}/N_{u,exp}$  is approximately 1.10, i.e., an ~10% overprediction of the experimental results by the numerical model. Figure 8 shows the observed experimental and numerical crack patterns as well as the load–displacement curves. The contour crack lines and solid thin lines represent the crack patterns obtained from the numerical simulations and the corresponding (typical) experimental observations, respectively. In all cases, the concrete cone angles are  $< 35^\circ$  ( $35^\circ$  is the angle suggested by the CCD model), and both the experimental and numerical results indicate a slight stripping of the top layer of the concrete paste. According to Fig. 8, for models 1–3, i.e., anchors with an embedment depth of 40 mm, the concrete cone size obtained experimentally ( $\alpha \approx 20^\circ$ ) is larger than the cone size obtained from the numerical analyses ( $\alpha \approx 27^\circ$ ), where  $\alpha$  is the failure cone angle. Similarly, the load–displacement curves obtained from numerical analyses show a slightly higher residual capacity after the peak load is reached compared to that of the anchors tested experimentally at  $h_{ef} = 40$  mm. For all other models, the concrete cone sizes and load–displacement graphs are in good agreement with the experimental results. Minor differences in the capacity of the anchors and the concrete cone angle can be related to any relative movement/slippage of the anchors in concrete, imperfections in the experiments, local non-homogeneity of the material, and frictional forces that are not simulated in the numerical models [9]. The numerical

models are therefore considered reliable for predicting not only the capacity of the anchors but also their relevant cone shape and crack patterns.

### 5.2 Comparison between the numerical results and theoretical prediction models

Comparing the values predicted using Eqs. (1) and (2) with the numerical results (Table 8), reveals that the CCD model overestimates the numerical capacities in all cases, and the extent of this overestimation varies significantly depending on the effective embedment depth. At an embedment depth of 40 mm, the maximum overestimation by Eq. (1) is 31%, whereas at 70 and 90 mm, the maximum overestimates are 20% and 10%, respectively. In contrast, the LFM model underestimates the anchor capacities in all cases, and the extent of the underestimation also depends on the effective embedment depth. However, the trend is in the opposite direction, i.e., the maximum underestimation of 44% occurs at the maximum embedment depth of 90 mm, and it drops to a maximum of only 14% at an embedment depth of 40 mm. Based on the above, two further assessments can be suggested: first, whether the exponent of  $h_{ef}^{1.5}$  in both the CCD and LFM models (i.e., reflecting the maximum possible size effect suggested by Bažant [104]) holds for anchors installed in geopolymers; second, whether the relationships commonly used for normal concrete to relate the modulus of elasticity and fracture energy to the compressive strength can be directly applied to geopolymers.

### 5.3 Comparison between anchors in normal and geopolymers (Serie B)

The numerical results for the anchors embedded in normal concrete (Serie B) are presented in Table 9. This table also includes the capacity of the anchors obtained using geopolymers ( $N_{u,geop}$ ) and the predicted values based on the CCD and LFM models. The results

**Table 7** Numerical and experimental results for Serie A

model No.	parameters and results				$N_{u,num}/N_{u,exp}$	$\alpha_{num} (^\circ)$	$\alpha_{exp} (^\circ)$
	WLL	$h_{ef}$ (mm)	$N_{u,num}$	$N_{u,exp}$			
1	1.3T	40	17.0	15.6	1.09	27	19
2	2.5T	40	17.7	17.0	1.04	28	20
3	5T	40	18.7	19.7	0.95	26	20
4	1.3T	70	46.2	41.3	1.12	23	20
5	2.5T	70	46.5	45.4	1.02	22	19
6	5T	70	48.9	48.7	1.00	21	20
7	2.5T	90	75.4	76.2	0.99	23	22
8	5T	90	80.0	78.2	1.02	24	23

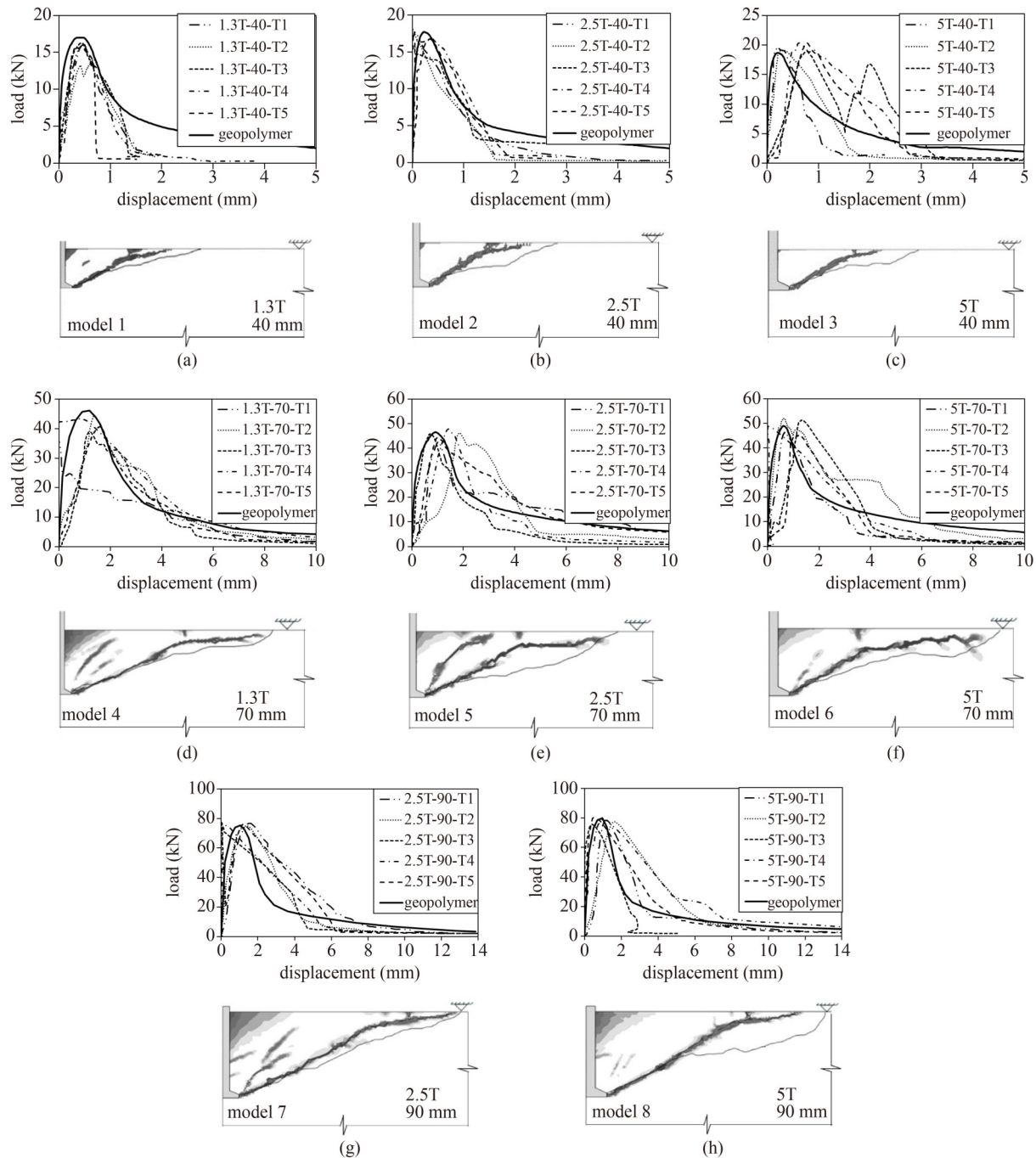


**Fig. 8** Comparisons between load–displacement graphs and crack patterns of anchors in the numerical analyses (models 1–8) and experimental results. (a) model 1; (b) model 2; (c) model 3; (d) model 4; (e) model 5; (f) model 6; (g) model 7; (h) model 8.

show that in all cases, the capacities of the anchors in normal concrete ( $N_{u,norm}$ ) are 30%–40% higher than those in geopolymer concrete. This outcome is mainly related to the difference in the mechanical properties of geopolymer and normal concrete; the elastic modulus and fracture energy of geopolymer concrete are, on average, 14% and 49% lower, respectively, than those of normal concrete (Table 1).

The concrete cone angles listed in Table 9 and the crack patterns shown in Fig. 9 indicate that the area of influence

of the concrete cone is approximately 40%–70% larger in geopolymer concrete than in normal concrete. The load–displacement curves shown in this figure also indicate a slightly stiffer behavior of anchors in normal concrete than in geopolymer concrete (i.e., anchors embedded in normal concrete consistently reach the maximum load at lower displacements than anchors in geopolymer concrete), which can directly be related to the higher elastic modulus of normal concrete. For the crack patterns shown in Fig. 9, the contour crack line

**Table 8** Comparison between numerical and theoretical prediction models

model No.	parameters and results			predicted capacities			comparisons	
	WLL	$h_{ef}$ (mm)	$N_{u,num}$	$N_{u,CCD}$	$N_{u,LFM}$	$N_{u,num}/N_{u,CCD}$	$N_{u,num}/N_{u,LFM}$	
1	1.3T	40	17.0	24.8	16.4	0.69	1.04	
2	2.5T	40	17.7	24.8	16.4	0.71	1.08	
3	5T	40	18.7	24.8	16.4	0.75	1.14	
4	1.3T	70	46.2	57.4	38.0	0.80	1.22	
5	2.5T	70	46.5	57.4	38.0	0.81	1.22	
6	5T	70	48.9	57.4	38.0	0.85	1.29	
7	2.5T	90	75.4	83.6	55.4	0.90	1.36	
8	5T	90	80.0	83.6	55.4	0.96	1.44	

**Table 9** Numerical results for Serie B analyses

model No.	parameters and results				predicted capacities		comparisons			$\alpha_{norm}$ (°)	$\alpha_{geop}$ (°)
	WLL	$h_{ef}$ (mm)	$N_{u,norm}$	$N_{u,geop}$	$N_{u,CCD}$	$N_{u,LFM}$	$N_{u,geop}/N_{u,norm}$	$N_{u,norm}/N_{u,CCD}$	$N_{u,norm}/N_{u,LFM}$		
9	1.3T	40	27.0	17.0	24.8	24.9	0.63	1.09	1.08	35	27
10	2.5T	40	28.6	17.7	24.8	24.9	0.62	1.15	1.15	36	28
11	5T	40	33.4	18.7	24.8	24.9	0.56	1.35	1.34	36	26
12	1.3T	70	69.9	46.2	57.4	57.6	0.66	1.22	1.21	33	23
13	2.5T	70	70.2	46.5	57.4	57.6	0.66	1.22	1.22	35	22
14	5T	70	72.2	48.9	57.4	57.6	0.68	1.26	1.25	32	21
15	2.5T	90	100.8	75.4	83.6	84.0	0.75	1.21	1.20	33	23
16	5T	90	111.6	80.0	83.6	84.0	0.72	1.33	1.33	35	24

shows the crack pattern of the anchor in normal concrete, and the solid thin line shows the crack pattern of the anchor in geopolymer concrete.

The results presented in Table 9 further demonstrate that both the CCD and LFM models underestimate the capacity of anchors in normal concrete by a margin of 9%–35%, which reinforces the suitability of both models for anchors installed in normal concrete, even though the difference is on the high side. Such a relatively high difference, however, can be associated with the larger anchor head sizes (lower anchor head size ratios) used in this series of analyses (compared to the anchors with small and medium head sizes used in the experiments to develop the two prediction models). A detailed investigation of the influence of the anchor head size on their tensile capacities in both geopolymer and normal concrete is provided in Subsection 5.5.

#### 5.4 Influence of surface cracking (Serie C)

The numerical results obtained by investigating the influence of the surface cracking are listed in Table 10, where  $N_{u,cr}$  is the ultimate tensile capacity of the anchor obtained from numerical simulations in cracked concrete. In this series of analyses, a crack with a width of 0.2 mm and depth of 10 mm is induced at different distances from the center of the anchor by introducing a discontinuity (U-shaped notch) in the mesh. This crack size was selected because it was the largest surface crack observed

in the experiments. The results show that the anchor capacity strongly depends on the effective embedment depth of the anchor and the location of the crack. As expected, the tensile capacity of the anchor is not affected to a meaningful level when the crack is located at  $L_{cr} = 0.5h_{ef}$  and  $1.0h_{ef}$ , that is, within the concrete cone footprint, in any cases. However, at  $L_{cr} = 1.5h_{ef}$ , most of the anchors show a meaningful change in both the cone size and ultimate capacity, depending on their embedment depths.

At an embedment depth of 40 mm, the tensile capacity is reduced by 33% when the crack is located at  $L_{cr} = 1.5h_{ef}$ . The reductions in the anchor capacities are 11% and only 1% at effective embedment depths of 70 mm and 90 mm, respectively. A clear change in the concrete cone crack pattern is observed for the anchors embedded at 40 and 70 mm at  $L_{cr} = 1.5h_{ef}$  (Fig. 10). Such changes in the shape of the concrete cones can be justified based on how the concrete cone is formed; during the analyses, it is observed that the concrete cone reaches ~30%–35% of its total height/lateral side when the anchor reaches ~90% of its ultimate capacity, which is similar to the observations made by Özbolt et al. [105]. Therefore, the anchors at an embedment depth of 40 mm are more susceptible to premature failure, i.e., a change in the direction of the crack as the cone forms, moving the cone cracks toward the induced crack, and hence leading to a smaller cone than those embedded at depths of 70 or 90 mm. Figure 10 shows the load–displacement curves and crack patterns of

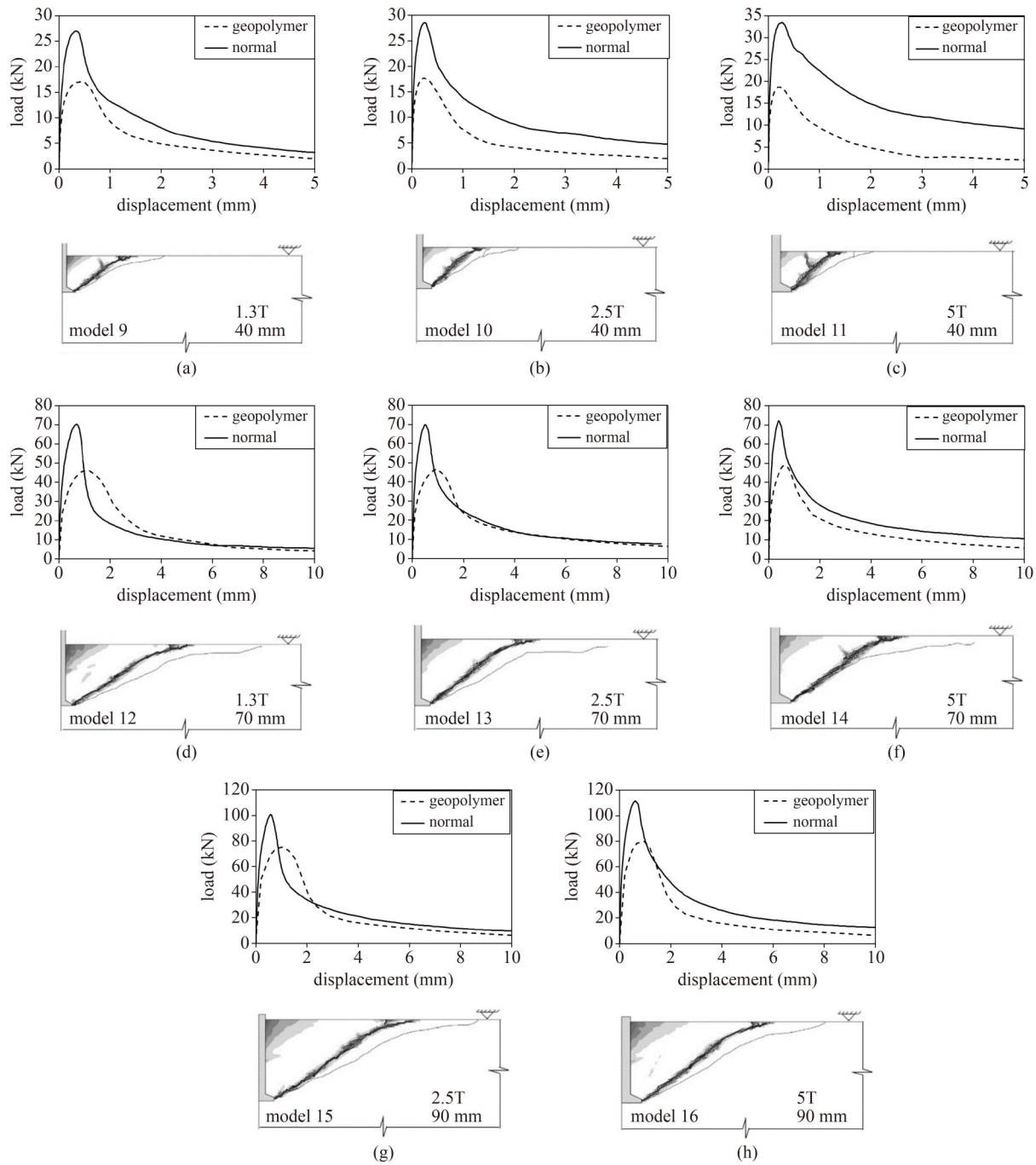


**Fig. 9** Comparisons between load–displacement curves and crack patterns of anchors from the numerical analyses in normal concrete and geopolymer concrete (models 9–16). (a) model 9; (b) model 10; (c) model 11; (d) model 12; (e) model 13; (f) model 14; (g) model 15; (h) model 16.

all of the models analyzed in this series. In Fig. 10, the solid thin line shows the crack pattern of the anchor in uncracked concrete. Based on the load–displacement curves, the anchors with an induced surface crack show a 40%–70% increase in displacement related to the peak load, whereas their post-peak behavior remains the same. It should be noted that although the results obtained from the numerical analyses are consistently lower than those of the experiment (i.e., on the safe side), for the reasons

explained in Subsection 4.1, they are still in good agreement with the experimental results. Therefore, the current numerical model provides a relatively simple tool (compared with a 3D model) that can reasonably predict the maximum effect of such cracks on the ultimate capacity of the anchors. An alternative could be a 3D model in which cracks of random lengths, widths, and depths (still based on experimental measurements) are introduced to create a more realistic representation of the

**Table 10** Numerical results for Serie C analyses

model No.	parameters and results					$N_{u,cr}/N_{u,geop}$	$\alpha_{cr} (^{\circ})$	$\alpha_{geop} (^{\circ})$
	WLL	$h_{ef}$ (mm)	$L_{cr}$	$N_{u,cr}$	$N_{u,geop}$			
17	2.5T	40	$0.5h_{ef}$	16.7	17.7	0.94	29	28
18	2.5T	40	$1.0h_{ef}$	16.4	17.7	0.93	28	28
19	2.5T	40	$1.5h_{ef}$	11.9	17.7	0.67	37	28
20	2.5T	70	$0.5h_{ef}$	48.5	46.5	1.04	23	22
21	2.5T	70	$1.0h_{ef}$	47.5	46.5	1.02	22	22
22	2.5T	70	$1.5h_{ef}$	41.4	46.5	0.89	34	22
23	2.5T	90	$0.5h_{ef}$	78.4	75.4	1.04	25	23
24	2.5T	90	$1.0h_{ef}$	77.2	75.4	1.02	25	23
25	2.5T	90	$1.5h_{ef}$	74.5	75.4	0.99	25	23

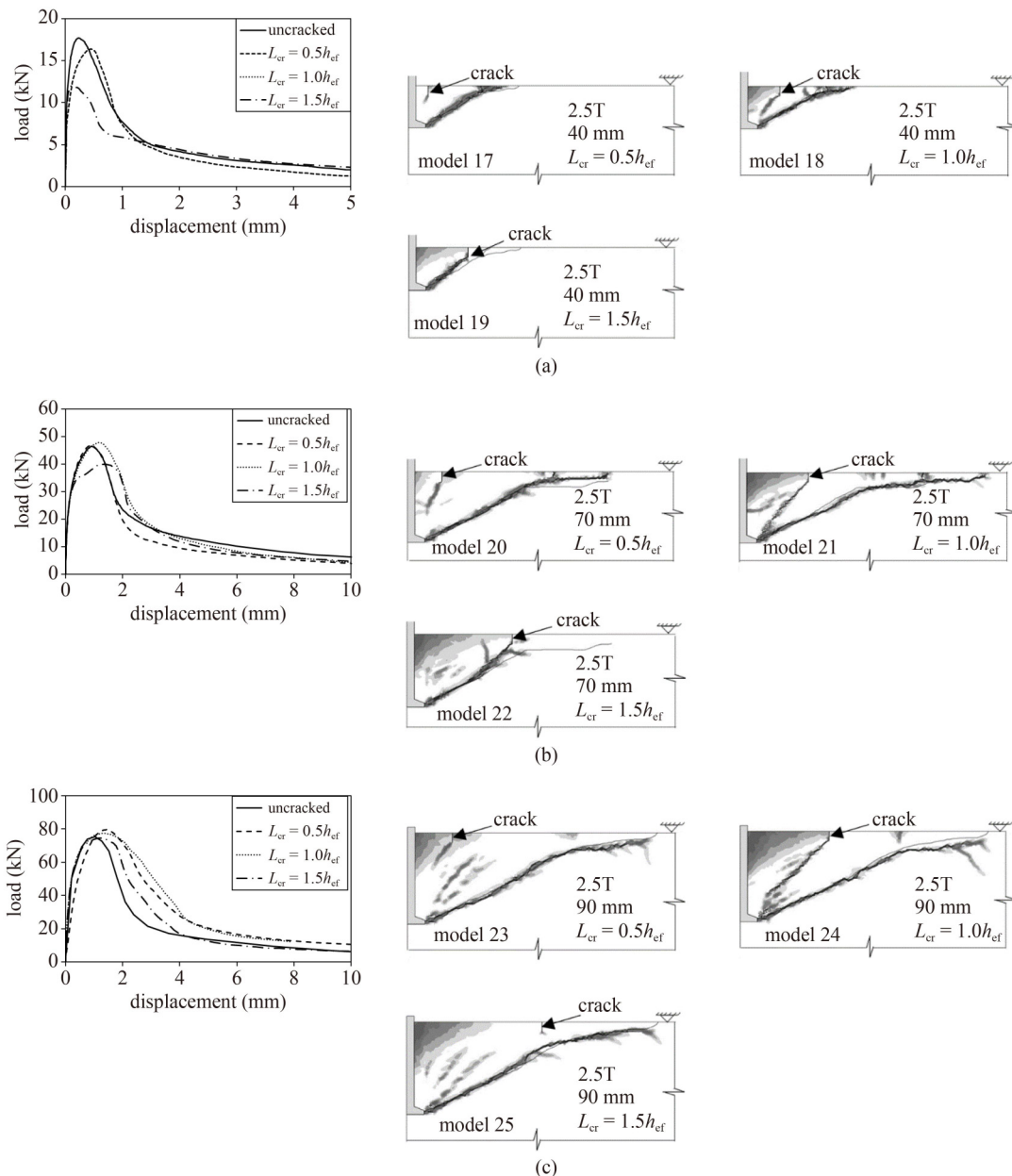


**Fig. 10** Comparisons between load–displacement curves and crack patterns of anchors from numerical analyses in geopolymer concrete with varying  $L_{cr}$  (models 17–25): (a)  $h_{ef} = 40$  mm; (b)  $h_{ef} = 70$  mm; (c)  $h_{ef} = 90$  mm.

actual cracks. However, this would result in a substantially more complex model, with perhaps not as substantial an added value.

5.5 Influence of the anchor profile (Serie D)

Table 11 presents the numerical results obtained from the analysis of type P2 anchors and compares these results with those for type P1 anchors discussed in Subsections 5.2 and 5.3. Similarly, Fig. 11 compares the crack patterns and load–displacement curves. In this table and figure,  $N_{u,P2}$  is the ultimate tensile capacity of the anchor obtained from numerical simulations using P2-type anchors and  $N_{u,P1}$  is the ultimate tensile capacity of the

anchor obtained from numerical simulations using P1-type anchors. The results indicate that at an effective embedment depth of 40 mm, the P1 anchors produce a 3%–6% higher capacity, which occurs at a displacement that is up to 10% greater than that of the P2 anchors. However, at an effective embedment depth of 90 mm, the P2 anchors show up to 4% higher capacities, occurring at a displacement that is 21% greater. These differences are insignificant and can be ignored. Moreover, in most cases, the crack patterns associated with the two profiles almost coincide with no significant differences. Therefore, it can be concluded that despite the speculations made at the start of this study based on the direction of the principal stresses in the vicinity of the head of the

Table 11 Numerical results for Serie D analyses

model No.	parameters and results					$N_{u,P2}/N_{u,P1}$	$\alpha_{P2}$ (°)	$\alpha_{P1}$ (°)
	WLL	$h_{ef}$ (mm)	concrete type	$N_{u,P2}$	$N_{u,P1}$			
26	2.5T	40	G	16.8	17.7	0.94	28	28
27	2.5T	40	N	27.7	28.6	0.97	36	36
28	2.5T	70	G	44.0	46.5	0.95	24	22
29	2.5T	70	N	70.9	70.2	1.01	35	35
30	2.5T	90	G	77.6	75.4	1.03	23	23
31	2.5T	90	N	104.6	100.8	1.04	33	33

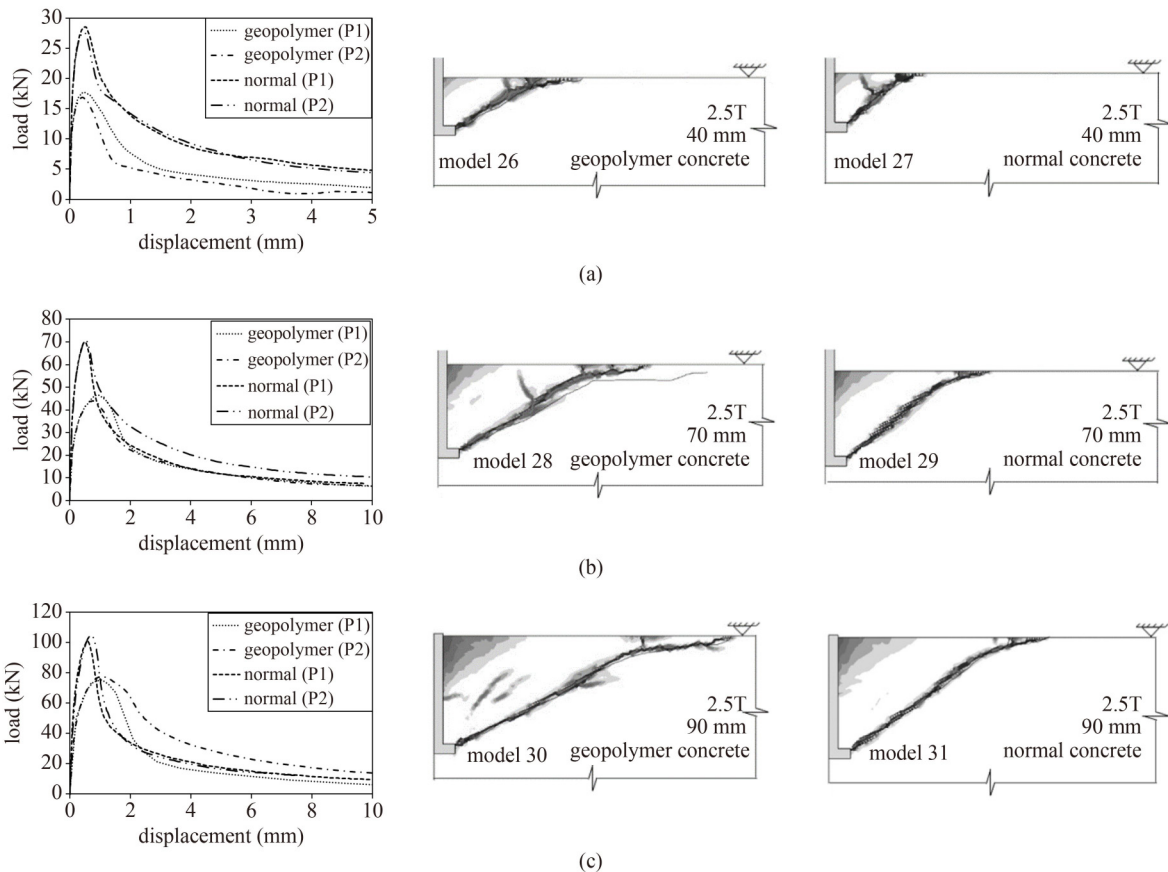


Fig. 11 Comparisons between load–displacement curves and crack patterns of anchors from numerical analyses in geopolymer and normal concrete with varying anchor profiles (models 26–31): (a)  $h_{ef}$  = 40 mm; (b)  $h_{ef}$  = 70 mm; (c)  $h_{ef}$  = 90 mm.

anchors, the difference in the anchor head profile does not influence the behavior of the anchor to any meaningful level, regardless of the concrete type. For the crack patterns shown in Fig. 11, the solid thin line and contour crack line show the crack patterns of the anchors with Profile 1 (P1) and Profile 2 (P2), respectively.

5.6 Influence of the anchor head size (Serie E)

The numerical results showing the variation in the capacity and concrete cone size of the anchors with varying anchor head size in both geopolymer and normal concrete are listed in Table 12. The capacity of the anchors in geopolymer concrete increases as the anchor head size increases from small to medium by an average of 6%, and the capacity increases by an average of 22% when the head size increases from small to large. In normal concrete, the anchor capacity increases by an average of 7% when the head size increases from small to medium and by an average of 20% when the head size increases from small to large. The general observations mentioned above, i.e., an increase in capacity as a result of an increase in head size, are in agreement with the results of other studies on normal concrete [35,37]. However, the numerical results presented in this study show up to 10% lower capacities than those reported by Nilforoush et al. [27], which is likely due to the surface

reinforcement in the concrete slabs used by Nilforoush et al. [27].

The CCD and LFM models overestimate or underestimate the capacity of all anchors embedded in geopolymer concrete, and the extent of the overestimation depends on the effective embedment depth of the anchors (as discussed in Subsection 5.2) and the anchor head size. As mentioned previously, the small-headed anchors show 6% and 22% lower capacities than the medium- and large-headed anchors, respectively. For the anchors embedded in normal concrete, the CCD and LFM models accurately predict the capacity of small- and medium-headed anchors but underestimate the capacity of large-headed anchors by up to 40% (as discussed in Subsection 5.3). Such variations are partly because neither the CCD nor LFM models include a factor that represents the effect of the anchor head size ratio. However, generally, these results are in good agreement with those of studies conducted on anchors with different head sizes [35,39].

Equation (3), which is based on the CCD and LFM models with an additional modification factor to consider the effect of the anchor head size, provides relatively accurate predictions for almost all of the analyses in normal concrete. For anchors in geopolymer concrete, when Eq. (3) and the LFM model are used, the predictions provide the lowest and closest results to those of the numerical analyses. This equation overestimates

**Table 12** Numerical results for Serie E analyses

model No.	parameters and results				predicted capacities						comparisons				$\alpha$ (°)
	$h_{ef}$ (mm)	concrete type	anchor		$N_u$	$N_{u,CCD}$	$N_{u,LFM}$	$N_{u,AH}$		$N_u/N_{u,CCD}$	$N_u/N_{u,LFM}$	$N_u/N_{u,AH}$			
			head size	$\sigma_b/f_c$				CCD	LFM			CCD	LFM		
32	40	G	S	20.0	13.9	24.8	16.4	23.9	16.5	0.56	0.85	0.58	0.84	44	
33	40	G	M	9.0	14.4	24.8	16.4	25.9	17.9	0.58	0.88	0.56	0.80	39	
26	40	G	L	0.9	16.8	24.8	16.4	32.7	22.7	0.68	1.02	0.51	0.74	28	
34	40	N	S	20.0	24.4	24.8	24.9	23.9	24.0	0.98	0.98	1.02	1.02	42	
35	40	N	M	9.0	26.5	24.8	24.9	25.9	26.0	1.07	1.06	1.02	1.02	42	
27	40	N	L	0.9	27.7	24.8	24.9	32.7	32.9	1.12	1.11	0.85	0.84	36	
36	70	G	S	20.0	36.1	57.4	38.0	55.9	35.2	0.63	0.95	0.65	1.03	47	
37	70	G	M	9.0	37.7	57.4	38.0	60.5	38.1	0.66	0.99	0.62	0.99	42	
28	70	G	L	2.1	44.0	57.4	38.0	69.9	48.3	0.77	1.16	0.63	0.91	24	
38	70	N	S	20.0	54.1	57.4	57.6	55.9	51.2	0.94	0.94	0.97	1.06	47	
39	70	N	M	9.0	58.6	57.4	57.6	60.5	55.3	1.02	1.02	0.97	1.06	45	
29	70	N	L	2.1	70.9	57.4	57.6	69.9	70.1	1.24	1.23	1.01	1.01	35	
40	90	G	S	20.0	62.2	83.6	55.4	83.3	49.4	0.74	1.12	0.75	1.26	47	
41	90	G	M	9.0	67.7	83.6	55.4	90.1	53.5	0.81	1.22	0.75	1.27	30	
30	90	G	L	3.0	77.6	83.6	55.4	97.8	67.8	0.93	1.40	0.79	1.14	23	
42	90	N	S	20.0	91.6	83.6	84.0	83.3	71.8	1.10	1.09	1.10	1.28	46	
43	90	N	M	9.0	94.2	83.6	84.0	90.1	77.6	1.13	1.12	1.05	1.21	41	
31	90	N	L	3.0	104.6	83.6	84.0	97.8	98.4	1.25	1.25	1.07	1.06	33	

Notes: S: small; M: medium; L: large.

the capacity of the anchors in geopolymer concrete at  $h_{ef} = 40$  mm by 26% and underestimates their capacities by 28% when embedded at  $h_{ef} = 90$  mm. Therefore, it can be concluded that the modification factor,  $\Psi_{AH}^{0.1}$ , used with the LFM, can capture the influence of the anchor head size ratio in both normal and geopolymer concrete. The difference in the numerical-to-predicted capacity ratios observed in geopolymer concrete can be related to the exponent  $h_{ef}^{1.5}$ , which does not seem to apply to anchors embedded in geopolymer concrete. Note that the numerical-to-prediction values (CCD and LFM models) are similar for all anchor head size ratios when the modification factor,  $\Psi_{AH}^{0.1}$ , is incorporated in the models; this indicates that the modification factor provided by Nilforoush et al. [35] accurately incorporates the effect of anchor head size ratios for both concrete types.

Figures 12–14 show the load–displacement curves and crack patterns of all anchors analyzed in Serie E. According to the load–displacement curves, as the head size increases (or the anchor head size ratio decreases), the anchors exhibit a stiffer response (i.e., the anchor displacement at the ultimate load decreases with an increase in the anchor head size). The crack patterns of the small- and medium-size anchors in both normal and geopolymer concrete and at all embedment depths show a steeper (larger) concrete cone angle compared with the

large-headed anchors. This is due to the high bearing stresses on the head of the anchors, and hence, the earlier local crushing of concrete in the case of small and medium anchor heads. The concrete cone diameter for small- and medium-headed anchors is less than  $3h_{ef}$  ( $\alpha > 35^\circ$ ), whereas for large-headed anchors, the concrete cone diameter in normal concrete is almost equal to  $3h_{ef}$  ( $\alpha \approx 35^\circ$ ); in geopolymer concrete, it is almost equal to  $5h_{ef}$ . Therefore, the minimum anchor-to-anchor spacing of  $3h_{ef}$  and edge distance of  $1.5h_{ef}$  considered by the CCD model require further investigation for anchors installed in geopolymer concrete.

For small-headed anchors, a secondary crack propagates, but it never reaches the surface to form a complete cone. Given that such secondary cracks do not appear to form in all cases, further investigations are required to understand when they form and how they may affect the ultimate capacities. Similar cracks were observed in the numerical results reported by Nilforoush et al. [35].

## 6 Conclusions and future recommendations

In this study, the concrete cone capacity and crack

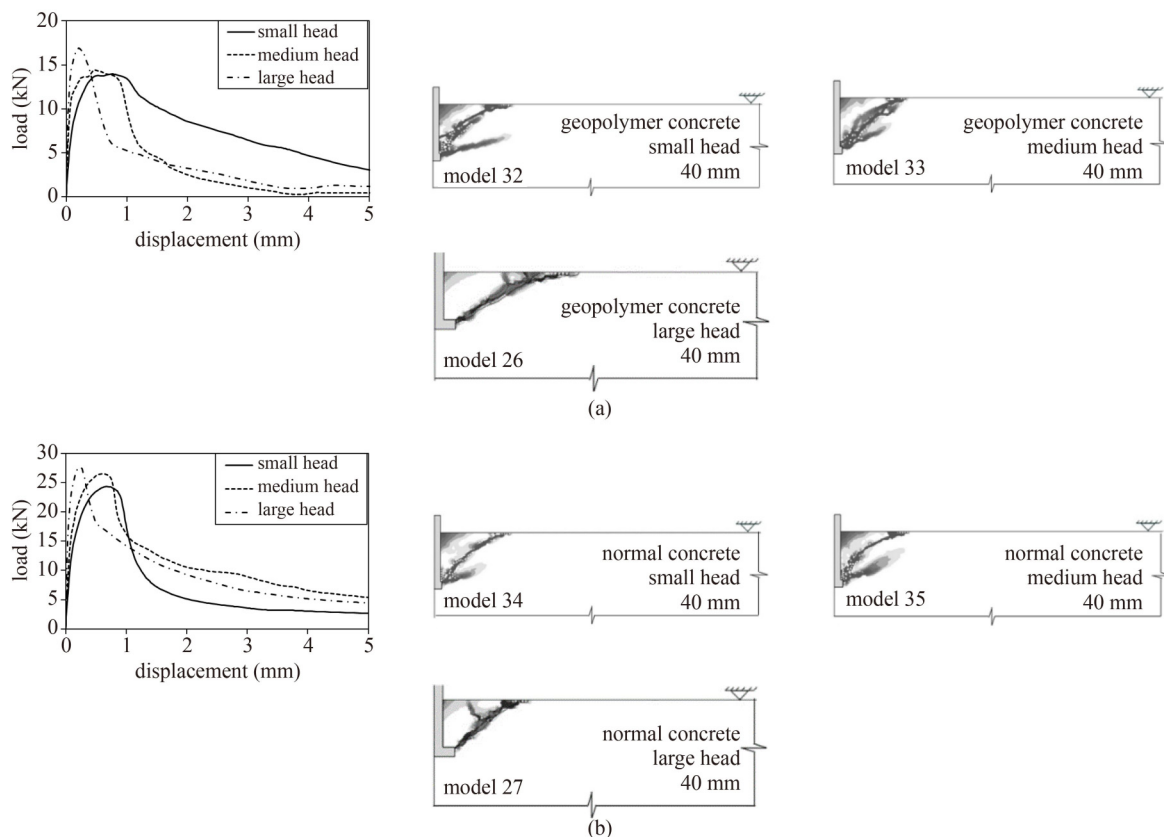


**Fig. 12** Comparisons between load–displacement curves and crack patterns of anchors from numerical analyses with varying anchor head sizes at  $h_{ef} = 40$  mm (models 26, 27, 32–35): (a) anchors in geopolymer concrete; (b) anchors in normal concrete.

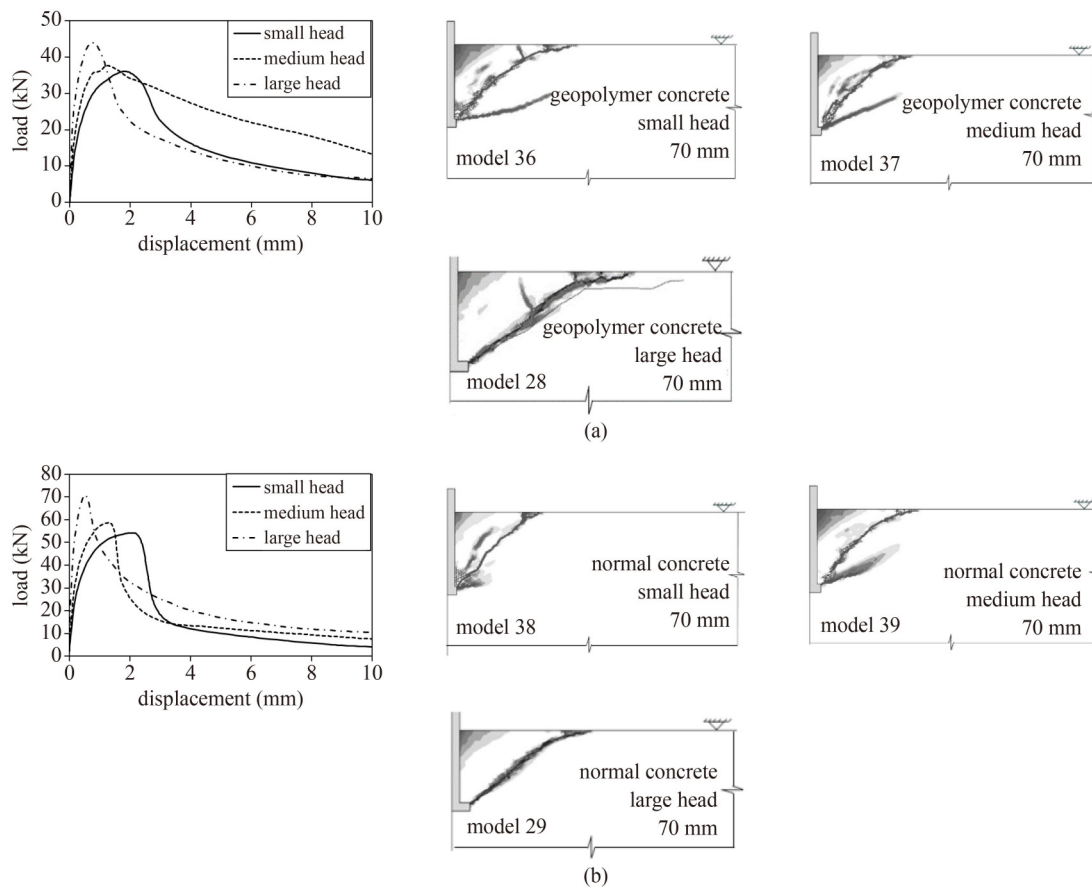


**Fig. 13** Comparisons between load–displacement curves and crack patterns of anchors from numerical analyses with varying anchor head sizes at  $h_{ef} = 70$  mm (models 28, 29, 36–39): (a) anchors in geopolymer concrete; (b) anchors in normal concrete.

patterns of cast-in headed anchors installed in geopolymer and normal concrete are investigated using numerical analyses. A total of 43 different analyses are conducted in five different series. Based on the results, the following conclusions can be drawn.

1) The CCD model overestimates the capacity of the anchors in geopolymer concrete. The extent of this overestimation depends on the effective embedment depth of the anchor and the anchor head size. At  $h_{ef} = 40$  mm, the CCD model overestimates the tensile capacity of the anchor by 44% and 32% for small and large head size anchors, respectively. At  $h_{ef} = 90$  mm, the CCD model overestimates the anchor capacity by 26% and 7% for small and large anchor heads, respectively.

2) The LFM model overestimates the capacity of anchors in geopolymer concrete at  $h_{ef} = 40$  mm by up to 15% and underestimates the capacity of the anchors by up to 23% and 40% at  $h_{ef} = 70$  and 90 mm, respectively. Similar to the CCD model, the LFM model does not include a modification factor to incorporate the influence of the head size ratio, resulting in the above variation.

3) The capacity of the anchors in geopolymer concrete increase at a greater rate with respect to the effective embedment depth compared with the above prediction

models. This indicates that the exponent  $h_{ef}^{1.5}$  does not apply to anchors embedded in geopolymer concrete.

4) The capacity of the anchors in geopolymer concrete increases by 6% and 22% when the head size increases from small to medium and large, respectively.

5) Compared to anchors in normal concrete of similar compressive strength, anchors with similar head sizes show a 30%–40% lower capacity and a concrete cone of 40%–70% larger diameter when installed in geopolymer concrete.

6) The magnitude of the reduction in the capacity of anchors installed in surface-cracked concrete depends on the effective embedment depth and location of the crack. The highest reduction in anchor capacity (33%) is observed for the anchor installed at  $h_{ef} = 40$  mm and  $L_{cr} = 1.5h_{ef}$ . There is also a 40%–70% increase in the displacement related to the peak load, i.e., less stiff behavior. The reduction in anchor capacity is not significant when the crack is located at distances of less than  $1.5h_{ef}$  from the anchor, as it does not cause the redirection of cracks toward the induced surface crack when the concrete cone forms. It should be noted that this study was conducted using 2D axisymmetric models; therefore, the influence of random surface cracking could not be investigated. A

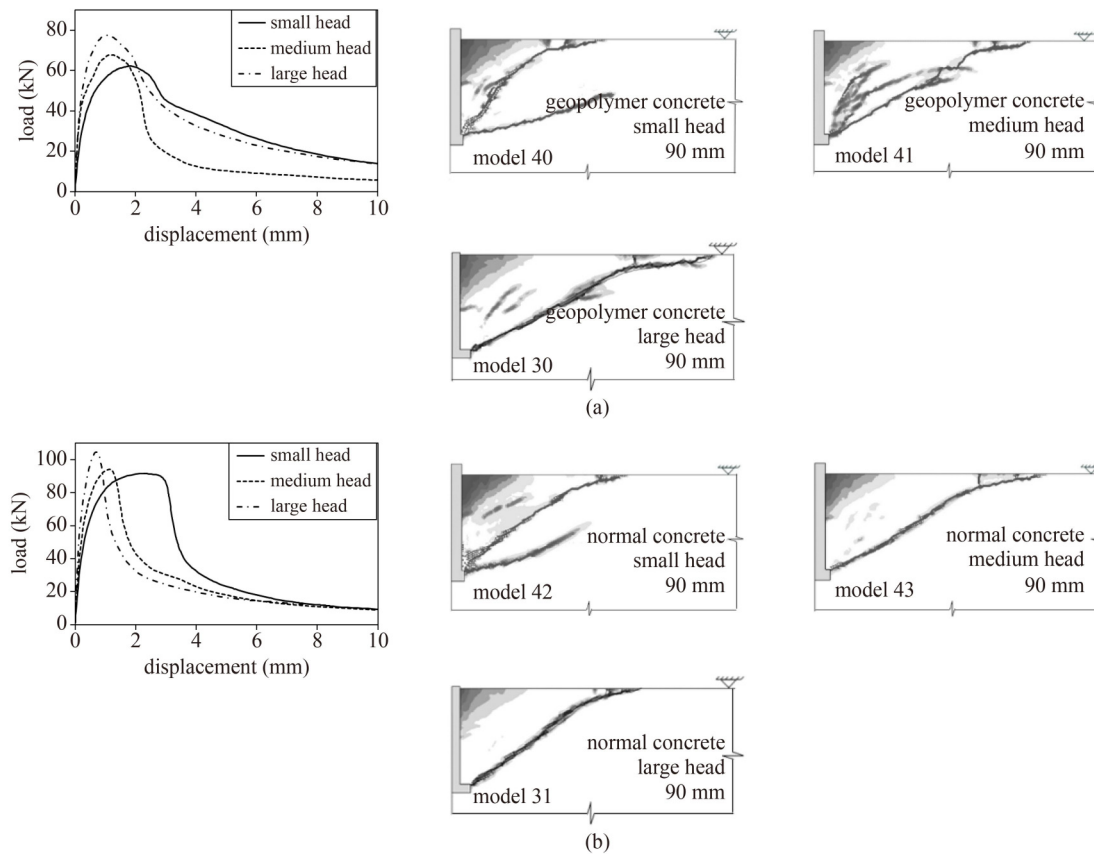


**Fig. 14** Comparisons between load–displacement curves and crack patterns of anchors from numerical analyses with varying anchor head sizes at  $h_{ef} = 90$  mm (models 30, 31, 40–43): (a) anchors in geopolymer concrete; (b) anchors in normal concrete.

3D model would facilitate such a study to better understand the impact of surface cracking on the behavior of anchors, whether in normal or other types of concrete.

7) No significant change in the tensile behavior of the anchors is observed with different head profiles (P1 and P2). Therefore, in future numerical studies, head profile P1 can be simplified to P2.

8) For the wide range of anchor head sizes and embedment depths considered in the current study, the modification factor suggested by Nilfouroush et al. [35] improves both the CCD and LFM models to accurately predict the tensile capacity of anchors installed in normal concrete. However, neither of the models can predict the capacity of anchors installed in geopolymer concrete accurately, with or without the above modification factor. Therefore, further studies are required to extend the application of these two models to anchors in geopolymer concrete.

9) The stress–strain relationships of the specific geopolymer concrete materials utilized in this study are defined based on experimental tests under both tension and compression. This is due to the lack of analytical models in the literature for such concrete. Therefore, more focused research on geopolymer concrete is required to develop generic constitutive material models for such construction materials.

**Open Access** This article is licensed under a Creative Commons Attribution 4.0 International License (<https://creativecommons.org/licenses/by/4.0/>), which permits use, sharing, adaptation, distribution and reproduction in any medium or format, as long as you give appropriate credit to the original author(s) and the source, provide a link to the Creative Commons licence, and indicate if changes were made. The images or other third party material in this article are included in the article's Creative Commons licence, unless indicated otherwise in a credit line to the material. If material is not included in the article's Creative Commons licence and your intended use is not permitted by statutory regulation or exceeds the permitted use, you will need to obtain permission directly from the copyright holder. To view a copy of this licence, visit <http://creativecommons.org/licenses/by/4.0/>.

**Funding note** Open Access funding enabled and organized by CAUL and its Member Institutions.

**Conflict of Interest** The authors declare that they have no conflict of interest.

## References

1. Eligehausen R, Mallee R, Silva J F. Anchorage in Concrete Construction. Berlin: Wilhelm Ernst & Sohn Verlag für Architektur und Technische Wissenschaften, 2006
2. ACI 349-01. Code Requirements for Nuclear Safety-Related

- Concrete Structures and Commentary. Farmington Hills, MI: ACI Committee 349, 2001
3. Eligehausen R, Sawade G. A Fracture Mechanics Based Description of the Pull-Out Behavior of Headed Studs Embedded in Concrete. OPUS—Publication Server of the University of Stuttgart, 1989
  4. Fuchs W, Eligehausen R, Breen J E. Concrete capacity design (CCD) approach for fastening to concrete. *ACI Structural Journal*, 1995, 92(1): 73
  5. ACI 318-19. Building Code Requirements for Structural Concrete and Commentary. Farmington Hills, MI: ACI Committee 318, 2019
  6. ACI 349-13. Code Requirements for Nuclear Safety-Related Concrete Structures and Commentary. Farmington Hills, MI: ACI Committee 349, 2013
  7. AS 3850.1:2015. Prefabricated Concrete Elements—General Requirements. Sydney: Standards Australia Committee, 2015
  8. EN 1992-4, Eurocode 2. Design of Concrete Structures. Design of Fastenings for Use in Concrete. London: BSI, 2018
  9. Piccinin R, Ballarini R, Cattaneo S. Pullout capacity of headed anchors in prestressed concrete. *Journal of Engineering Mechanics*, 2012, 138(7): 877–887
  10. Piccinin R, Ballarini R, Cattaneo S. Linear elastic fracture mechanics pullout analyses of headed anchors in stressed concrete. *Journal of Engineering Mechanics*, 2009, 136(6): 761–768
  11. Nilforoush R, Nilsson M, Elfgren L. Experimental evaluation of tensile behaviour of single cast-in-place anchor bolts in plain and steel fibre-reinforced normal- and high-strength concrete. *Engineering Structures*, 2017, 147: 195–206
  12. Primavera E J, Pinelli J P, Kalajian E H. Tensile behavior of cast-in-place and undercut anchors in high-strength concrete. *Structural Journal*, 1997, 94(5): 583–594
  13. Toth M, Bokor B, Sharma A. Anchorage in steel fiber reinforced concrete—Concept, experimental evidence and design recommendations for concrete cone and concrete edge breakout failure modes. *Engineering Structures*, 2019, 181: 60–75
  14. Choi S, Joh C, Chun S C. Behavior and strengths of single cast-in anchors in Ultra-High-Performance Fiber-Reinforced Concrete (UHPFRC) subjected to a monotonic tension or shear. *KSCSE Journal of Civil Engineering*, 2015, 19(4): 964–973
  15. McMackin P J. Headed steel anchor under combined loading. *Engineering Journal*, 1973, 43–52
  16. Mohyeddin A, Lee J. Behaviour of Screw Anchors and Drop-in Anchors in Bubble Deck Slabs. Internal ECU Report. 2018
  17. Schwenn M, Voit K, Zeman O, Bergmeister K. Post-installed mechanical fasteners in high strength and ultra-high strength performance concrete. *Civil Engineering Design*, 2019, 1(5–6): 161–167
  18. Gesoglu M, Özturan T, Özel M, Güneyisi E. Tensile behavior of post-installed anchors in plain and steel fiber-reinforced normal- and high-strength concretes. *ACI Structural Journal*, 2005, 102(2): 224
  19. Mohyeddin A, Gad E, Lee J. Tensile capacity of screw anchors due to the pull-out failure mode. In: 5th International fib Congress. Melbourne: Federation Internationale du Beton (fib), 2019
  20. Mohyeddin A, Gad E, Lee J, Hafsia M, Saremi M. Adverse effect of too-small edge distances on tensile capacity of screw anchors. *Australian Journal of Structural Engineering*, 2020, 21(1): 94–106
  21. Eligehausen R, Mattis L, Wollmershauser R, Hoehler M S. Testing anchors in cracked concrete. *Concrete International*, 2004, 26(7): 66–71
  22. Nilforoush R, Nilsson M, Elfgren L, Özbolt J, Hofmann J, Eligehausen R. Influence of surface reinforcement, member thickness, and cracked concrete on tensile capacity of anchor bolts. *ACI Structural Journal*, 2017, 114(6): 114
  23. Kim S Y, Yu C S, Yoon Y S. Sleeve-type expansion anchor behavior in cracked and uncracked concrete. *Nuclear Engineering and Design*, 2004, 228(1–3): 273–281
  24. Lee S, Jung W. Evaluation of structural performance of post-installed anchors embedded in cracked concrete in power plant facilities. *Applied Sciences*, 2021, 11(8): 3488
  25. Baran E, Schultz A, French C. Tension tests on cast-in-place inserts: the influence of reinforcement and prestress. *PCI Journal*, 2006, 51(5): 88–108
  26. Nilsson M, Ohlsson U, Elfgren L. Effects of surface reinforcement on bearing capacity of concrete with anchor bolts. *Cement and Concrete Research*, 2011, 2011(44): 161–174
  27. Nilforoush R, Nilsson M, Elfgren L. Experimental evaluation of influence of member thickness, anchor-head size, and orthogonal surface reinforcement on the tensile capacity of headed anchors in uncracked concrete. *Journal of Structural Engineering*, 2018, 144(4): 04018012
  28. Winters J B, Dolan C W. Concrete breakout capacity of cast-in-place concrete anchors in early-age concrete. *PCI Journal*, 2014, 59(1): 114–131
  29. Al-Yousuf A, Pokharel T, Lee J, Gad E, Abdouka K, Sanjayan J. Performance of cast-in anchors in early age concrete with supplementary cementitious materials. *Materials and Structures*. 2023, 56(1):1–5
  30. Barraclogh A. Analysis of edgelifft anchor failures in experimental precast panels. Dissertation for the Doctoral Degree. Perth: Curtin University, 2016
  31. Krešimir Nincevic L M C M M, Roman W W. Age and cure dependence of concrete cone capacity in tension. *ACI Structural Journal*, 2019, 116(4): 91–100
  32. Obayes O, Gad E, Pokharel T, Lee J, Abdouka K. Evaluation of concrete material properties at early age. *CivilEng*, 2020, 1(3): 326–350
  33. Mohyeddin A, Gad E, Khandu R, Yangdon K, Lee J, Ismail M. Screw anchors installed in early age concrete. In: *Mechanics of Structures and Materials XXIV: Proceedings of the 24th Australian Conference on the Mechanics of Structures and Materials*. Perth: CRC Press, 2019
  34. Mohyeddin A, Gad E F, Yangdon K, Khandu R, Lee J. Tensile load capacity of screw anchors in early age concrete. *Construction & Building Materials*, 2016, 127: 702–711
  35. Nilforoush R, Nilsson M, Elfgren L, Özbolt J, Hofmann J, Eligehausen R. Tensile capacity of anchor bolts in uncracked concrete: influence of member thickness and anchor's head size. *ACI Structural Journal*, 2017, 114(6): 1519–1530

36. Barraclough A, Moeinaddini F. Pull-out capacity of cast-in headed anchors in prefabricated concrete elements. In: 3rd International Symposium on Connections between Steel and Concrete Stuttgart. Stuttgart: Institute of Construction Material, 2017
37. Eligehausen R, Bouska P, Cervenka V, Pukl R. Fracture Mechanics of Concrete Structures. London: CRC Press, 1992, 517–525
38. Ožbolt J, Eligehausen R, Periškić G, Mayer U. 3D FE analysis of anchor bolts with large embedment depths. Engineering Fracture Mechanics, 2007, 74(1–2): 168–178
39. Lee N H, Kim K S, Bang C J, Park K R. Tensile-headed anchors with large diameter and deep embedment in concrete. ACI Structural Journal, 2007, 104(4): 479
40. di Nunzio G, Marchisella A, Muciaccia G. The effect of very low bearing pressure on the behavior of cast-in anchors. In: 9th International Conference on Concrete Under Severe Conditions-Environment and Loading. Porto Alegre: Unisinos University, 2019
41. Cook R A. Behavior of chemically bonded anchors. Journal of Structural Engineering, 1993, 119(9): 2744–2762
42. Ronald A C, Robert C K. Factors influencing bond strength of adhesive anchors. ACI Structural Journal, 2001, 98(1): 76–86
43. Higgins C C, Klingner R E. Effects of environmental exposure on the performance of cast-in-place and retrofit anchors in concrete. Structural Journal, 1998, 95(5): 506–517
44. Lahouar M A, Caron J F, Pinoteau N, Forêt G, Benzarti K. Mechanical behavior of adhesive anchors under high temperature exposure: Experimental investigation. International Journal of Adhesion and Adhesives, 2017, 78: 200–211
45. Mohyeddin A, Gad E, Aria S, Lee J. Effect of thread profile on tensile performance of screw anchors in non-cracked concrete. Construction & Building Materials, 2020, 237: 117565
46. Karmokar T, Mohyeddin A, Lee J, Paraskeva T. Concrete cone failure of single cast-in anchors under tensile loading: A literature review. Engineering Structures, 2021, 243: 112615
47. DiNunzio G, Muciaccia G. A literature review of the head-size effect on the capacity of cast-in anchors. In: 10th International Conference on Fracture Mechanics of Concrete and Concrete Structures—Proceedings. Bayonne: FraMCoS, 2019
48. Tóth M, Bokor B, Sharma A. Comprehensive literature review on anchorages in steel fibre reinforced concrete. In: Concrete Structures: New Trends for Eco-Efficiency and Performance. Lisbon: FIB Symposium, 2021
49. Anderson N S, Meinheit D F. A review of headed stud design criteria in the sixth edition PCI design handbook. PCI Journal, 2007, 52(1): 82
50. Cheok G S, Phan L T. Post-Installed Anchors. A Literature Review. NIST Interagency/Internal Report (NISTIR). Gaithersburg: National Institute of Standards and Technology, 1998
51. Rolf E, Tamas B. Behavior of Fasteners Loaded in Tension in Cracked Reinforced Concrete. ACI Structural Journal, 1995, 92(3): 365–379
52. Eligehausen R. Behavior, Design and Testing of Anchors in Cracked Concrete. Detroit, MI: ACI Publication, 1991
53. Kuenzel C, Vandeperre L J, Donatello S, Boccaccini A R, Cheeseman C. Ambient temperature drying shrinkage and cracking in metakaolin-based geopolymers. Journal of the American Ceramic Society, 2012, 95(10): 3270–3277
54. Zuhua Z, Xiao Y, Huajun Z, Yue C. Role of water in the synthesis of calcined kaolin-based geopolymer. Applied Clay Science, 2009, 43(2): 218–223
55. Sharma C, Jindal B B. Effect of variation of fly ash on the compressive strength of fly ash based geopolymer concrete. IOSR Journal of Mechanical and Civil Engineering, 2015, 42–44
56. Cong P, Cheng Y. Advances in geopolymer materials: A comprehensive review. Journal of Traffic and Transportation Engineering, 2021, 8(3): 283–314
57. Bouaissi A, Li L Y, Al Bakri Abdullah M M, Bui Q B. Mechanical properties and microstructure analysis of FA-GGBS-HMNS based geopolymer concrete. Construction & Building Materials, 2019, 210: 198–209
58. Deb P S, Nath P, Sarker P K. The effects of ground granulated blast-furnace slag blending with fly ash and activator content on the workability and strength properties of geopolymer concrete cured at ambient temperature. Materials & Design, 2014, 62: 32–39
59. Nath P, Sarker P. Geopolymer concrete for ambient curing condition. In: The Australasian Structural Engineering Conference 2012 (ASEC 2012). Perth: Engineers Australia, 2021
60. Alrefaei Y, Wang Y S, Dai J G. The effectiveness of different superplasticizers in ambient cured one-part alkali activated pastes. Cement and Concrete Composites, 2019, 97: 166–174
61. Yousefi Oderji S, Chen B, Ahmad M R, Shah S F A. Fresh and hardened properties of one-part fly ash-based geopolymer binders cured at room temperature: Effect of slag and alkali activators. Journal of Cleaner Production, 2019, 225: 1–10
62. Ren J, Sun H, Li Q, Li Z, Zhang X, Wang Y, Li L, Xing F. A comparison between alkali-activated slag/fly ash binders prepared with natural seawater and deionized water. Journal of the American Ceramic Society, 2022, 105(9): 5929–5943
63. Xie J, Kayali O. Effect of superplasticiser on workability enhancement of Class F and Class C fly ash-based geopolymers. Construction & Building Materials, 2016, 122: 36–42
64. Rashad A M. A comprehensive overview about the influence of different additives on the properties of alkali-activated slag—A guide for civil engineer. Construction & Building Materials, 2013, 47: 29–55
65. Bilim C, Karahan O, Atiş C D, Ilkentapar S. Influence of admixtures on the properties of alkali-activated slag mortars subjected to different curing conditions. Materials & Design, 2013, 44: 540–547
66. Nguyen T T, Goodier C I, Austin S A. Factors affecting the slump and strength development of geopolymer concrete. Construction & Building Materials, 2020, 261: 119945
67. Saha S, Rajasekaran C. Enhancement of the properties of fly ash based geopolymer paste by incorporating ground granulated blast furnace slag. Construction & Building Materials, 2017, 146: 615–620
68. Mathew G, Issac B M. Effect of molarity of sodium hydroxide on the aluminosilicate content in laterite aggregate of laterised

- geopolymer concrete. *Journal of Building Engineering*, 2020, 32: 101486
69. Mortar N A M, Kamarudin H, Rafiza R, Meor T, Rosnita M. Compressive strength of fly ash geopolymer concrete by varying sodium hydroxide molarity and aggregate to binder ratio. In: *IOP Conference Series: Materials Science and Engineering*. Philadelphia, PE: IOP Publishing, 2020
  70. Krishna Rao A, Kumar D R. Effect of various alkaline binder ratio on geopolymer concrete under ambient curing condition. *Materials Today: Proceedings*, 2020, 27: 1768–1773
  71. Elyamany H E, Abd Elmoaty A E M, Elshaboury A M. Setting time and 7-day strength of geopolymer mortar with various binders. *Construction & Building Materials*, 2018, 187: 974–983
  72. Ghafoor M T, Khan Q S, Qazi A U, Sheikh M N, Hadi M N S. Influence of alkaline activators on the mechanical properties of fly ash based geopolymer concrete cured at ambient temperature. *Construction & Building Materials*, 2021, 273: 121752
  73. Huang G, Yang K, Sun Y, Lu Z, Zhang X, Zuo L, Feng Y, Qian R, Qi Y, Ji Y, Xu Z. Influence of NaOH content on the alkali conversion mechanism in MSWI bottom ash alkali-activated mortars. *Construction & Building Materials*, 2020, 248: 118582
  74. Tuyan M, Andiç-Çakir Ö, Ramyar K. Effect of alkali activator concentration and curing condition on strength and microstructure of waste clay brick powder-based geopolymer. *Composites. Part B, Engineering*, 2018, 135: 242–252
  75. Fernandez-Jimenez A M, Palomo A, Lopez-Hombrados C. Engineering properties of alkali-activated fly ash concrete. *ACI Materials Journal*, 2006, 103(2): 106
  76. Muhammad N, Baharom S, Amirah N, Ghazali M, Alias N. Effect of heat curing temperatures on fly ash-based geopolymer concrete. *International Journal of Engineering & Technology*, 2019, 8(1.2): 15–19
  77. Jindal B B, Parveen D, Singhal D, Goyal A. Predicting relationship between mechanical properties of low calcium fly ash-based geopolymer concrete. *Transactions of the Indian Ceramic Society*, 2017, 76(4): 258–265
  78. Tayeh B A, Zeyad A M, Agwa I S, Amin M. Effect of elevated temperatures on mechanical properties of lightweight geopolymer concrete. *Case Studies in Construction Materials*, 2021, 15: e00673
  79. Memon F A, Nuruddin M F, Demie S, Shafiq N. Effect of curing conditions on strength of fly ash-based self-compacting geopolymer concrete. *International Journal of Civil and Environmental Engineering*, 2011, 5(8): 342–345
  80. Nath P, Sarker P K. Flexural strength and elastic modulus of ambient-cured blended low-calcium fly ash geopolymer concrete. *Construction & Building Materials*, 2017, 130: 22–31
  81. Aisheh Y I A, Atrushi D S, Akeed M H, Qaidi S, Tayeh B A. Influence of steel fibers and microsilica on the mechanical properties of ultra-high-performance geopolymer concrete (UHP-GPC). *Case Studies in Construction Materials*, 2022, 17: e01245
  82. Mousavinejad S H G, Gashti M F. Effects of alkaline solution to binder ratio on fracture parameters of steel fiber reinforced heavyweight geopolymer concrete. *Theoretical and Applied Fracture Mechanics*, 2021, 113: 102967
  83. Karimipour A, de Brito J. Influence of polypropylene fibres and silica fume on the mechanical and fracture properties of ultra-high-performance geopolymer concrete. *Construction & Building Materials*, 2021, 283: 122753
  84. Aldred J, Day J. Is geopolymer concrete a suitable alternative to traditional concrete. In: *Proceedings of the 37th Conference on Our World in Concrete & Structures*. Singapore: CI-Premier Pte, 2012
  85. Le Minh H, Khatir S, Abdel Wahab M, Cuong-Le T. A concrete damage plasticity model for predicting the effects of compressive high-strength concrete under static and dynamic loads. *Journal of Building Engineering*, 2021, 44: 103239
  86. Eriksson D, Gasch T. *FEM-modeling of Reinforced Concrete and Verification of the Concrete Material Models Available in ABAQUS*. Stockholm: Royal Institute of Technology, 2010
  87. Xu Z, Huang Y, Liang R. Numerical simulation of lap-spliced ultra-high-performance concrete beam based on bond-slip. *Buildings*, 2022, 12(8): 1257
  88. Smith M. *ABAQUS/Standard User's Manual, Version 6.9*, 2009
  89. Alfarah B, López-Almansa F, Oller S. New methodology for calculating damage variables evolution in plastic damage model for RC structures. *Engineering Structures*, 2017, 132: 70–86
  90. Nguyen G D, Korsunsky A M. Development of an approach to constitutive modelling of concrete: Isotropic damage coupled with plasticity. *International Journal of Solids and Structures*, 2008, 45(20): 5483–5501
  91. CEB-FIP. *Model Code 2010*. Switzerland: Comité Euro-International du Béton, 2010
  92. Hordijk D A. Tensile and tensile fatigue behaviour of concrete—Experiments, modeling and analyses. *Heron*, 1992, 37(1): 3–79
  93. Phillips D, Binsheng Z. Direct tension tests on notched and un-notched plain concrete specimens. *Magazine of Concrete Research*, 1993, 45(162): 25–35
  94. Karmokar T, Mohyeddin A, Lee J. Tensile behaviour of cast-in headed anchors in ambient-temperature cured geopolymer concrete. *Engineering Structures*, 2022, 266: 114643
  95. Bažant Z P, Oh B H. Crack band theory for fracture of concrete. *Materiales de Construcción*, 1983, 16(3): 155–177
  96. Hillerborg A, Modéer M, Petersson P E. Analysis of crack formation and crack growth in concrete by means of fracture mechanics and finite elements. *Cement and Concrete Research*, 1976, 6(6): 773–781
  97. Xenos D, Grassl P. Modelling the failure of reinforced concrete with nonlocal and crack band approaches using the damage-plasticity model CDPM2. *Finite Elements in Analysis and Design*, 2016, 117–118: 11–20
  98. Genikomsou A S, Polak M A. Finite element analysis of punching shear of concrete slabs using damaged plasticity model in ABAQUS. *Engineering Structures*, 2015, 98: 38–48
  99. Sümer Y, Aktaş M. Defining parameters for concrete damage plasticity model. *Challenge Journal of Structural Mechanics*, 2015, 1(3): 149–155
  100. Szczecina M, Winnicki A. Selected aspects of computer modeling of reinforced concrete structures. *Archives of Civil Engineering*, 2016, 62(1): 51–64
  101. Zheng S, Liu Y, Liu Y, Zhao C. Experimental and parametric

- study on the pull-out resistance of a notched perfobond shear connector. *Applied Sciences*, 2019, 9(4): 764
102. Malm R. Predicting shear type crack initiation and growth in concrete with non-linear finite element method. Dissertation for the Doctoral Degree. Stockholm: KTH Royal Institute of Technology, 2009
103. Wosatko A, Winnicki A, Polak M A, Pamin J. Role of dilatancy angle in plasticity-based models of concrete. *Archives of Civil and Mechanical Engineering*, 2019, 19(4): 1268–1283
104. Bažant Z P. Size effect in blunt fracture: Concrete, rock, metal. *Journal of Engineering Mechanics*, 1984, 110(4): 518–535
105. Ožbolt J, Eligehausen R, Reinhardt H W. Size effect on the concrete cone pull-out load. *International Journal of Fracture*, 1999, 391–404